

Optical Fourier surfaces

<https://doi.org/10.1038/s41586-020-2390-x>

Received: 18 December 2019

Accepted: 31 March 2020

Published online: 24 June 2020

 Check for updates

Nolan Lassaline¹, Raphael Brechbühler¹, Sander J. W. Vonk^{1,2}, Korneel Ridderbeek¹, Martin Spieser³, Samuel Bisig³, Boris le Feber¹, Freddy T. Rabouw^{1,2} & David J. Norris¹✉

Gratings¹ and holograms² use patterned surfaces to tailor optical signals by diffraction. Despite their long history, variants with remarkable functionalities continue to be developed^{3,4}. Further advances could exploit Fourier optics⁵, which specifies the surface pattern that generates a desired diffracted output through its Fourier transform. To shape the optical wavefront, the ideal surface profile should contain a precise sum of sinusoidal waves, each with a well defined amplitude, spatial frequency and phase. However, because fabrication techniques typically yield profiles with at most a few depth levels, complex ‘wavy’ surfaces cannot be obtained, limiting the straightforward mathematical design and implementation of sophisticated diffractive optics. Here we present a simple yet powerful approach to eliminate this design–fabrication mismatch by demonstrating optical surfaces that contain an arbitrary number of specified sinusoids. We combine thermal scanning-probe lithography^{6–8} and templating⁹ to create periodic and aperiodic surface patterns with continuous depth control and sub-wavelength spatial resolution. Multicomponent linear gratings allow precise manipulation of electromagnetic signals through Fourier-spectrum engineering¹⁰. Consequently, we overcome a previous limitation in photonics by creating an ultrathin grating that simultaneously couples red, green and blue light at the same angle of incidence. More broadly, we analytically design and accurately replicate intricate two-dimensional moiré patterns^{11,12}, quasicrystals^{13,14} and holograms^{15,16}, demonstrating a variety of previously unattainable diffractive surfaces. This approach may find application in optical devices (biosensors¹⁷, lasers^{18,19}, metasurfaces⁴ and modulators²⁰) and emerging areas in photonics (topological structures²¹, transformation optics²² and valleytronics²³).

A patterned optical surface can be described as a Fourier sum of sinusoidal waves. Each component represents a specific spatial frequency ($g = 2\pi/\lambda$ with period λ) that interacts with an impinging beam. For applications, diffractive surfaces should ideally contain only the frequencies of interest. However, they are typically obtained by etching patterns into surfaces to a fixed depth, creating arrays of vertical elements (trenches, holes and pillars) dictated by fabrication rather than design. This not only contributes unwanted spatial frequencies, complicating the optical response, but restricts the number of desired Fourier components that can be included. Appropriate placement of the elements (for example, aperiodically^{10,13,14,18}) can offer some additional control. Alternatively, the collective response from arrays of smaller elements—nanoscale, subwavelength resonators—can be exploited in metasurfaces²⁴. However, no approach has yet offered complete control over the Fourier components in a diffractive surface. If such an approach were available, simple analytical formulas could immediately specify the sum of sinusoids needed to obtain a complex desired output.

Wavy surfaces are in principle achievable using greyscale lithography²⁵, which spatially adjusts the exposure of a polymeric resist to produce patterns with multiple depth levels. The surface profile can then be transferred into the underlying substrate via etching. However,

greyscale lithography has not yet provided sufficient spatial resolution or depth control to create arbitrary optical surfaces. Similarly, interference lithography, which exposes the resist to multiple overlapping optical beams, can generate complex diffractive surfaces^{26,27}. But they contain at most a few spatial frequencies, constrained by the exposure wavelengths.

To obtain arbitrary control over the Fourier components, we first designed our structure by taking the Fourier transform of the desired diffraction pattern. After converting this analytical function into a two-dimensional (2D) greyscale bitmap (8-bit depth with 10 nm × 10 nm pixels; see Methods and Extended Data Fig. 1), we then use thermal scanning-probe lithography^{6–8} to raster-scan a heated cantilever with a sharp tip across a polymer film, locally removing material to match the bitmap depth at each pixel. The simultaneous monitoring of the surface topography by the tip for feedback means that arbitrary surfaces with sub-nanometre depth control and high spatial resolution (<100 nm) can be written at about 6 s μm^{-2} . These profiles can provide diffractive elements directly or be used as an etch mask or template. We exploit templating to replicate the pattern in other materials⁹.

Figure 1 demonstrates our approach with sinusoidal gratings modulated in one dimension (1D, periodic in x , constant in y), templated into silver (Ag), with one, two or three Fourier components

¹Optical Materials Engineering Laboratory, Department of Mechanical and Process Engineering, ETH Zurich, Zurich, Switzerland. ²Debye Institute for Nanomaterials Science, Utrecht University, Utrecht, The Netherlands. ³Heidelberg Instruments Nano/SwissLitho, Zurich, Switzerland. ✉e-mail: d.norris@ethz.ch

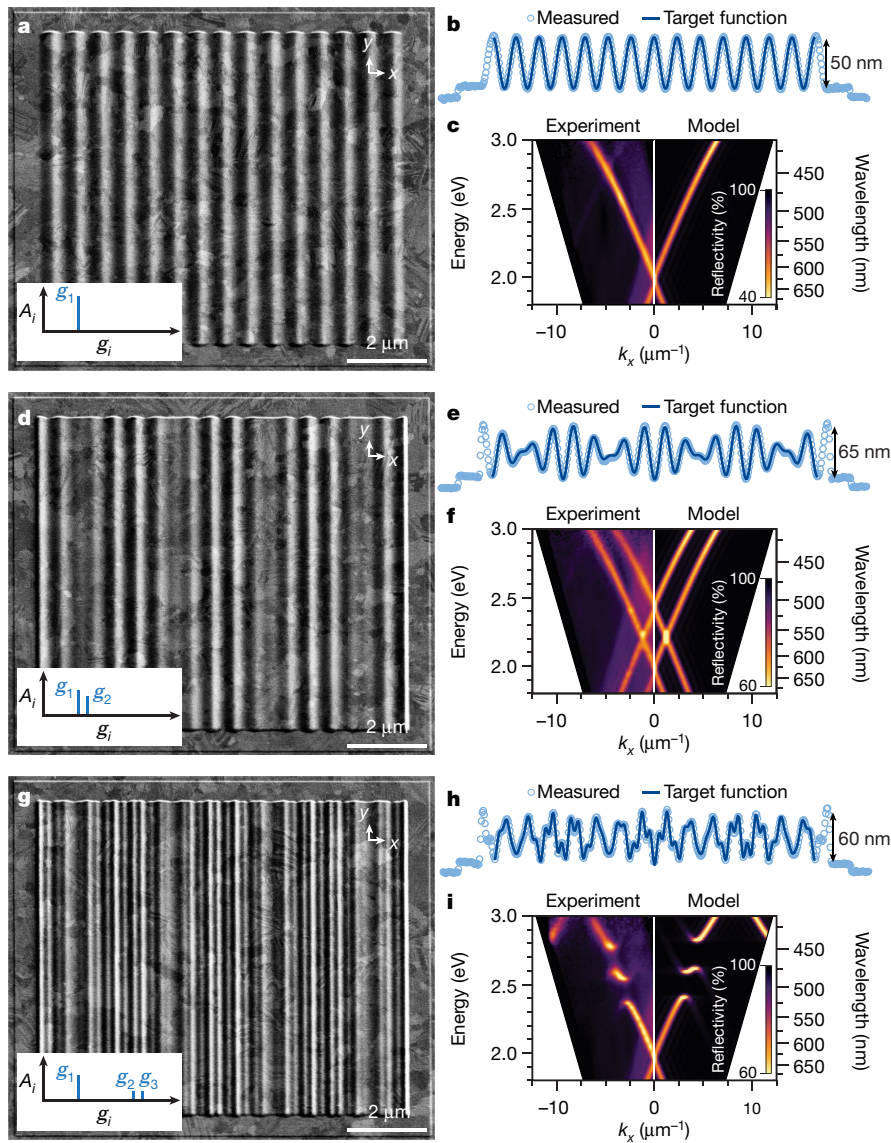


Fig. 1 | Fourier surfaces modulated in one dimension. **a, d, g.** Scanning-electron micrographs (SEMs, 30° tilt) of Ag gratings with 1, 2 or 3 sinusoidal components. The insets show the sinusoidal amplitudes A_i and spatial frequencies g_i . All design parameters are given in Extended Data Table 1. **b, e, h.** Measured (atomic force microscopy) and targeted surface topographies for the structures in **a, d** and **g**. Scan lengths are 11.3 μm and represent a single line in the structures. All target functions account for a slight distance miscalibration in the thermal scanning probe. The measured RMS error for the patterns are 1.8 nm, 2.1 nm and 2.3 nm, respectively (see Methods). **c.** Experimental (left) and modelled (right)

(Fig. 1a, d, g). Ag was chosen as a low-loss metal to explore non-transparent reflective gratings. The insets show the targeted amplitudes, A_i , and spatial frequencies, g_i , for sinusoid i (see the Methods for the analytical formulas for all surfaces). Because our structures are finite in size, their Fourier spectra will be slightly broader than in the analytical design (see modelling in Methods). The measured topographies for the patterns (Fig. 1b, e, h) show that the process faithfully reproduces the targeted profile with 1.8–2.3 nm root-mean-square (RMS) error (see Methods and Extended Data Fig. 2). These low values indicate that the desired Fourier components are dominant. Indeed, a detailed analysis for the single sinusoid (Extended Data Fig. 2) shows that the second harmonic is the largest error component with an amplitude of only 3.5% of A_1 (0.9 nm).

To test the optical response of our gratings, we measure angle-resolved reflectivity spectra by imaging the back focal plane of

angle-resolved reflectivity spectra (energy versus in-plane photon wavevector along the grating, k_x , with $k_y \approx 0$) for the structure in **a**. The orange lines represent decreased reflectivity at photon angles that launch surface plasmon polaritons (SPPs). These lines trace the SPP dispersion, displaced into the light cone by g_i . The black region represents energies and angles accessible in experiment (Extended Data Fig. 3). **f.** The two-component grating provides two photon–SPP coupling channels, doubling the orange lines. **i.** The three-component grating was designed to exhibit two plasmonic stopbands.

an optical microscope onto a spectrometer^{28,29} (Methods; Extended Data Fig. 3a). Each sinusoidal component (here periodic in x) can provide momentum $\mathbf{g}_i = (2\pi/A_i)\hat{\mathbf{x}}$ (where $\hat{\mathbf{x}}$ is the unit vector along x) to an impinging beam. These contributions can affect the outgoing angle of the radiation or lead to electromagnetic surface waves—surface plasmon polaritons (SPPs)—that propagate along the Ag–air interface with in-plane wavevector \mathbf{k}_{SPP} . We use the latter process (photon–SPP coupling) to characterize the capabilities of our surfaces.

We measure reflectivity as a function of the in-plane wavevector \mathbf{k}_{\parallel} of the incoming light. Figure 1c plots results for the single-sinusoidal grating for $\mathbf{k}_{\parallel} = k_x\hat{\mathbf{x}}$ (that is, energy versus k_x with $k_y \approx 0$; see Extended Data Fig. 3b). A linear polarizer was used to select only p-polarized light, which couples to SPPs (Methods). Decreased reflectivity (orange lines) occurs when $\mathbf{k}_{\parallel} \pm \mathbf{g}_i = \mathbf{k}_{\text{SPP}}$. Thus, the grating creates a photon–SPP coupling channel, allowing the plasmonic dispersion to be optically

probed. The match between the data and our analytical model (Fig. 1c; Methods), both here and below, confirms the fidelity of our process. See also Extended Data Fig. 4.

By including additional Fourier components, increasingly complex diffractive surfaces can be constructed. With two spatial frequencies \mathbf{g}_1 and \mathbf{g}_2 (Fig. 1d, e), two photon–SPP coupling channels open (Fig. 1f). Furthermore, SPP–SPP coupling arises if one of the spatial frequencies satisfies $\mathbf{k}_{\text{SPP}} \pm \mathbf{g}_i = \mathbf{k}'_{\text{SPP}}$, where \mathbf{k}_{SPP} and \mathbf{k}'_{SPP} are wavevectors for SPPs propagating in different in-plane directions. This leads to a plasmonic stopband^{30,31} (Extended Data Fig. 3b). Extended Data Fig. 5 shows an example at $\mathbf{k}_{\parallel} = 0$ when $\mathbf{g}_2 = 2\mathbf{g}_1$. Although we have focused so far on the spatial frequencies of the sinusoids, our fabrication approach also allows independent control of their phase and amplitude. In Extended Data Fig. 5, phase is used to render either the upper or lower stopband edge ‘dark’ (not coupled to photons)³⁰. Extended Data Fig. 6 uses amplitude to tune the stopband width (in energy) from 0 eV to about 0.5 eV. More generally, by adding further sinusoids, more complex plasmonic dispersions can be obtained. For example, Fig. 1g shows a three-component grating that results in multiple stopbands. These can be placed at arbitrary energies and incident photon angles. Although the surface profile (Fig. 1h) would be difficult to intuit, Fourier design followed by our process leads directly to the desired response (Fig. 1i). When such Fourier surfaces are converted into conventional two-depth-level gratings, the response is corrupted by unwanted spatial frequencies (Extended Data Fig. 4).

The control of sinusoidal components, shown above for patterns modulated in 1D with all \mathbf{g}_i along $\hat{\mathbf{x}}$, can be extended to patterns modulated in 2D (Extended Data Fig. 7a, b). For example, if we sum two sinusoids, one with \mathbf{g}_1 along $\hat{\mathbf{x}}$ and the other with \mathbf{g}_2 rotated by 10° from $\hat{\mathbf{x}}$, we obtain the moiré spatial interference pattern in Fig. 2a. For a 40° rotation, the pattern in Fig. 2b results. Because these gratings now provide in-plane momentum along both $\hat{\mathbf{x}}$ and $\hat{\mathbf{y}}$, we plot reflectivity versus in-plane wavevector components k_x and k_y , taking a fixed-energy slice from the full dispersion diagram (Extended Data Fig. 3c). The linear polarizer used in Fig. 1 was removed (Methods). The experimentally accessible wavevectors for such a ‘ k -space image’ (due to our finite collection angle) are within the solid white circles in Fig. 2c, d. The measured reflectivity exhibits two pairs of orange arcs, each pair representing solutions to $\mathbf{k}_{\parallel} \pm \mathbf{g}_i = \mathbf{k}_{\text{SPP}}$ (Extended Data Fig. 3d). Both plots (Fig. 2c, d) also include the 2D Fourier transform of the surface profile; the Fourier components $\pm\mathbf{g}_1$ and $\pm\mathbf{g}_2$ appear as orange spots outside the white circle and quantitatively explain the measured arcs. Even for only a 10° rotation, which leads to subtle intricacies in the surface pattern (Fig. 2a), the expected diffraction is observed.

Our approach can also exploit different basis functions. Extended Data Fig. 7c, d shows a circular sinusoidal grating and a moiré interference pattern generated from two such gratings. Functions with varying local spatial frequencies can also be employed. Figure 2e shows a sinusoidal ‘zone plate’ (Methods). In general, such structures can act as Fresnel lenses to focus electromagnetic radiation by diffraction, representing a unit of holographic information. Here, our zone plates have dimensions appropriate for X-ray optics^{32,33}, with the added benefit of continuous depth control, highly desirable for this application³⁴.

While the number of spatial components is arbitrary, several important symmetries can be generated by combining only a few sinusoids. Figure 3a, b shows a periodic pattern created from three sinusoids with 60° rotation between them. The resulting profile is hexagonal, with sixfold rotational symmetry, a typical design for 2D arrays of holes or pillars. However, in our structure, the 2D Fourier spectrum is specified. The corresponding k -space image (Fig. 3c) reveals six orange arcs from photon–SPP coupling. Figure 3d, e shows a surface with 12-fold rotational symmetry created from six sinusoids with 30° rotation between them. In k -space, 12 orange arcs appear (Fig. 3f). This profile, which does not possess translational symmetry, would be quasiperiodic if infinitely extended. Similar photonic quasicrystals using quasiperiodic arrays

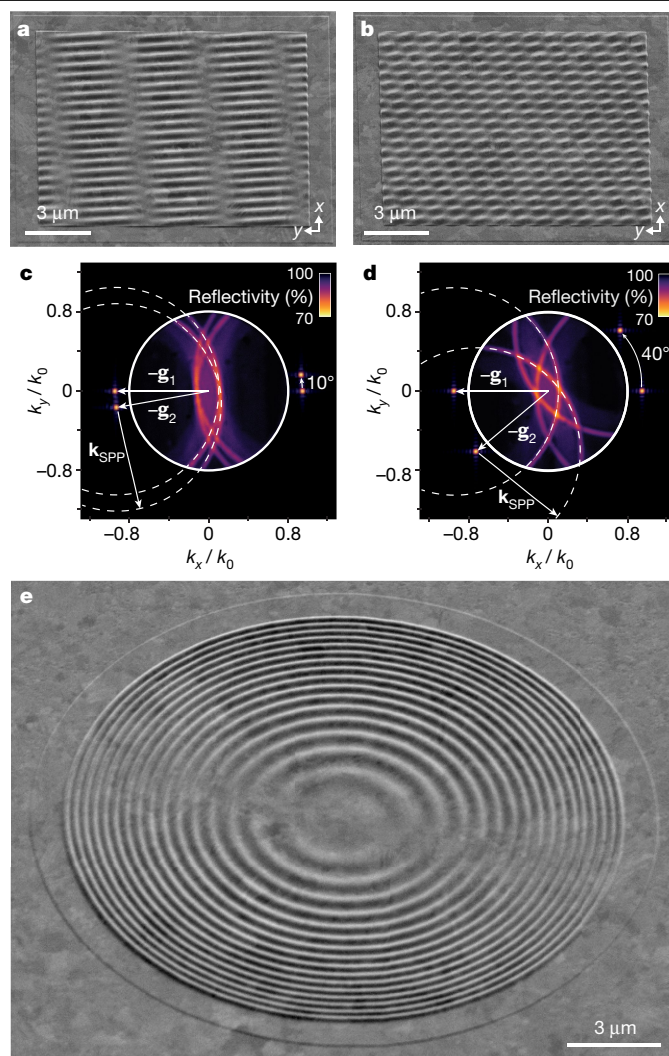


Fig. 2 | Fourier surfaces modulated in two dimensions. a, b, SEMs (45° tilt) of moiré patterns in Ag from two superimposed sinusoids: one with \mathbf{g}_1 along $\hat{\mathbf{x}}$ and the other with \mathbf{g}_2 rotated by 10° or 40° from $\hat{\mathbf{x}}$, respectively. See Extended Data Fig. 7. c, d, Measured k -space images (inside solid white circles) for photons (570 nm wavelength) reflected from patterns in a and b, respectively. k_x and k_y are normalized by the magnitude of the photon wavevector, k_0 . Four orange arcs appear, caused by decreased reflectivity when photons launch SPPs with wavevector \mathbf{k}_{SPP} , that is, when $\mathbf{k}_{\parallel} \pm \mathbf{g}_i = \mathbf{k}_{\text{SPP}} \pm \mathbf{g}_i$ and $\pm\mathbf{g}_2$ are shown as orange points outside the white circles. Their positions are determined from the 2D Fourier transform of the surface profiles used to define the structures. In c and d, we see that $\mathbf{k}_{\parallel} = -\mathbf{g}_2 + \mathbf{k}_{\text{SPP}}$ forms an orange arc in k -space. e, SEM (45° tilt) of a Ag sinusoidal zone plate. For all structural design parameters, see Extended Data Table 1.

of trenches or holes have been reported for laser applications^{10,18,35}. However, optimizing their design is computationally intensive and still results in 2D Fourier spectra with many unwanted spatial frequencies. Our structures are designed with simple analytical functions and exhibit precise control over the Fourier components.

To demonstrate the utility of our approach, we address a current limitation in photonics. The push for miniaturized optical systems has led to waveguides integrated into a single thin layer that exploits diffractive optics for in- and outcoupling of light^{20,36}. For these devices, multiple wavelengths should ideally be diffracted between free-space beams and propagating waveguide modes at a common angle. However, current single-spatial-frequency gratings cause them to diffract at different, highly specific angles, resulting in bigger, more complicated devices.

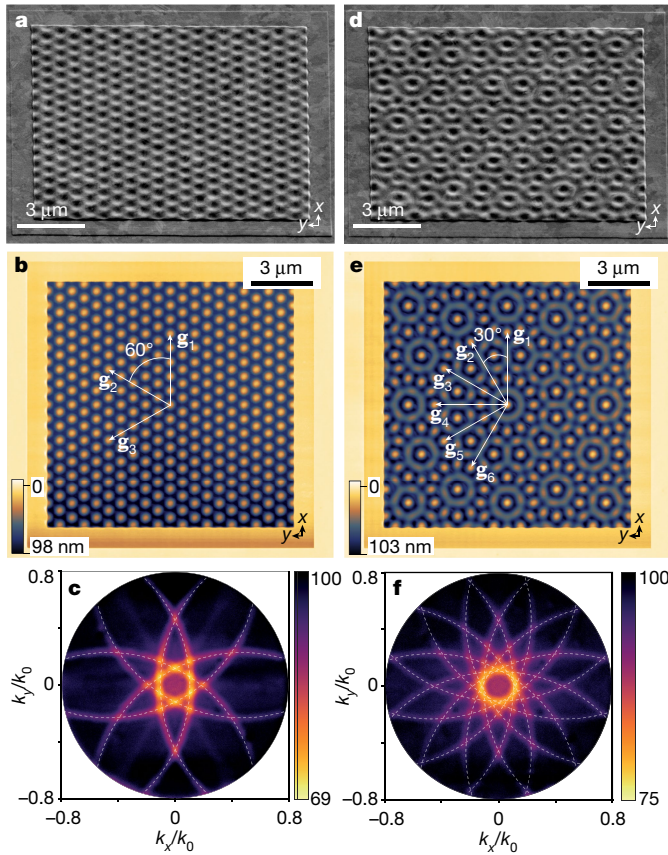


Fig. 3 | Periodic and quasiperiodic Fourier surfaces. **a, d**, SEMs (45° tilt) of periodic and quasiperiodic optical Fourier surfaces templated in Ag with 6- and 12-fold rotational symmetry, defined when three and six sinusoids are superimposed, respectively. **b, e**, Measured topographies (obtained during patterning) for the polymer films (PMMA/MA; see Methods) used to template the structures in **a** and **d**, respectively. All sinusoids have $\Lambda = 600$ nm and their corresponding vectors \mathbf{g}_i are oriented in-plane, as shown, spaced by 60° and 30°, respectively. **c, f**, Measured k -space reflectivity images for photons (570 nm wavelength) incident on the patterns in **a** and **d**, respectively. Six and 12 orange arcs appear, caused by decreased reflectivity when photons launch SPPs with wavevector \mathbf{k}_{SPP} , that is, when $\mathbf{k}_i \pm \mathbf{g}_i = \mathbf{k}_{\text{SPP}}$ (dashed white lines). k_x and k_y are normalized by the magnitude of the photon wavevector, k_0 . For all structural design parameters, see Extended Data Table 1.

With Fourier surfaces, a simple solution is immediately available. Three spatial frequencies can be included on a single surface to diffract three colours at a common angle. Figure 4a, b shows such a profile, designed, implemented and templated in Ag. The three sinusoidal components simultaneously couple red, green and blue photons at normal incidence (Fig. 4c), as seen by the three reflectivity dips in Fig. 4d, which arise due to photon–SPP coupling.

Additional applications of optical Fourier surfaces can benefit from deeper structures and a diverse material library. We patterned polymers of various refractive index (Methods) up to about 300 nm deep. When these deeper surfaces are templated into Ag, the resulting Fourier surfaces can provide efficient diffraction gratings (Extended Data Fig. 8). For a p-polarized beam at normal incidence, we measured $97 \pm 5\%$ in the +1 and –1 diffraction orders for a single-component sinusoidal grating. With two sinusoidal components, a ‘blazed’ Fourier surface is obtained that diffracts nearly all intensity into just the +1 diffraction order. The polymer profiles can also be transferred into substrates via etching, for example silicon (Si; Fig. 4e) or silicon nitride (SiN_x; Extended Data Fig. 9). With this we could amplify the profile depth⁸. Like the patterned polymer, the etched substrate can provide a multi-use

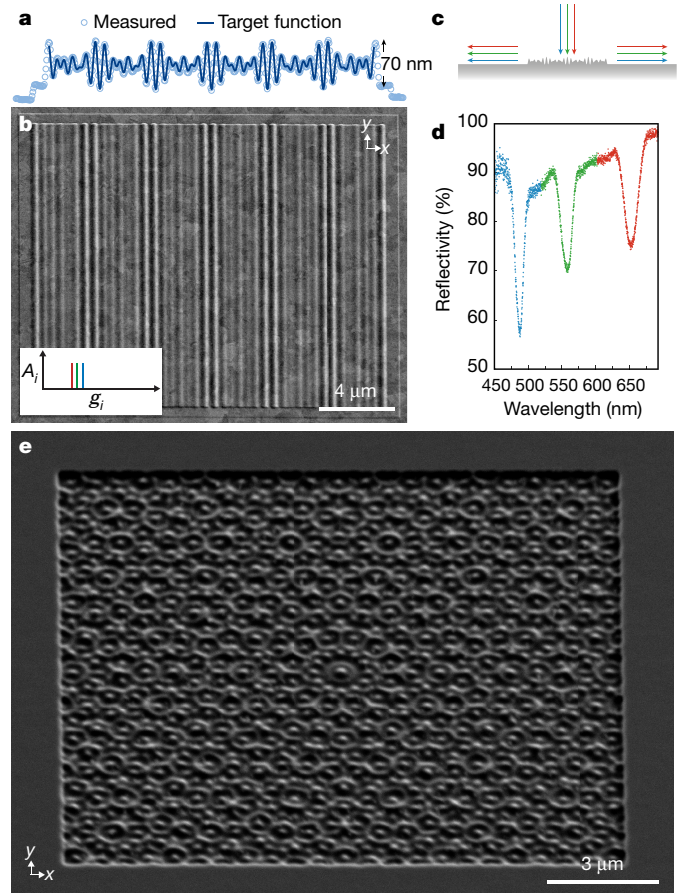


Fig. 4 | Applications of Fourier surfaces. **a**, Comparison of the measured (atomic force microscopy) and targeted surface topography (accounting for a slight distance miscalibration in the thermal scanning probe) for a Ag Fourier surface that couples red, green and blue photons at normal incidence to SPPs. Scan length is 22.0 μm . The profile contains three sinusoids with design periods $\Lambda_1 = 620$ nm, $\Lambda_2 = 520$ nm and $\Lambda_3 = 445$ nm. **b**, SEM (30° tilt) of the Ag Fourier surface in **a**. The inset shows the sinusoidal amplitudes A_i and spatial frequencies \mathbf{g}_i . All design parameters are given in Extended Data Table 1. **c**, Cartoon of the coupling of red, green and blue light simultaneously at normal incidence. **d**, Measured reflectivity as a function of photon wavelength for light at normal incidence (within $\pm 0.25^\circ$). The three prominent reflectivity dips (coloured as a visual guide) correspond to the coupling of red, green and blue light at normal incidence. **e**, SEM (45° tilt) of a 12-fold rotationally symmetric quasicrystal, defined with twelve sinusoids, etched into Si. For design parameters, see Extended Data Table 1.

template⁹. Extended Data Fig. 9 shows a titania (TiO₂) Fourier surface templated from an etched Si substrate.

Thus, ‘wavy’ diffractive surfaces can be provided for a broad spectral range (X-ray to infrared). Templating, extendable to rollable substrates³⁷, enables high-throughput production of many materials including active and multilayer solids^{38,39}. Optical wavefronts can be manipulated (including direction, phase and polarization^{40,41}) with diffractive surfaces that can be accurately placed within or on top of elements in integrated photonic devices, allowing miniaturized optical systems^{20,36}. Thus, researchers in photonics can exploit the previously unavailable capabilities of optical Fourier surfaces to address applications as well as to explore emerging phenomena.

Online content

Any methods, additional references, Nature Research reporting summaries, source data, extended data, supplementary information,

acknowledgements, peer review information; details of author contributions and competing interests; and statements of data and code availability are available at <https://doi.org/10.1038/s41586-020-2390-x>.

- Hopkinson, F. & Rittenhouse, D. An optical problem, proposed by Mr. Hopkinson, and solved by Mr. Rittenhouse. *Trans. Am. Phil. Soc.* **2**, 201–206 (1786).
- Gabor, D. A new microscopic principle. *Nature* **161**, 777–778 (1948).
- Ebbesen, T. W., Lezec, H. J., Ghaemi, H. F., Thio, T. & Wolff, P. A. Extraordinary optical transmission through sub-wavelength hole arrays. *Nature* **391**, 667–669 (1998).
- Khorasaninejad, M. et al. Metalenses at visible wavelengths: diffraction-limited focusing and subwavelength resolution imaging. *Science* **352**, 1190–1194 (2016).
- Goodman, J. W. *Introduction to Fourier Optics* (W. H. Freeman, 2017).
- Mamin, H. J. & Rugar, D. Thermomechanical writing with an atomic force microscope tip. *Appl. Phys. Lett.* **61**, 1003–1005 (1992).
- Pires, D. et al. Nanoscale three-dimensional patterning of molecular resists by scanning probes. *Science* **328**, 732–735 (2010).
- Rawlings, C. D. et al. Control of the interaction strength of photonic molecules by nanometer precise 3D fabrication. *Sci. Rep.* **7**, 16502 (2017).
- Nagpal, P., Lindquist, N. C., Oh, S. H. & Norris, D. J. Ultrasoft patterned metals for plasmonics and metamaterials. *Science* **325**, 594–597 (2009).
- Blanchard, R. et al. Gratings with an aperiodic basis: single-mode emission in multi-wavelength lasers. *New J. Phys.* **13**, 113023 (2011).
- Sunku, S. S. et al. Photonic crystals for nano-light in moiré graphene superlattices. *Science* **362**, 1153–1156 (2018).
- Wang, P. et al. Localization and delocalization of light in photonic moiré lattices. *Nature* **577**, 42–46 (2020).
- Matsui, T., Agrawal, A., Nahata, A. & Vardeny, Z. V. Transmission resonances through aperiodic arrays of subwavelength apertures. *Nature* **446**, 517–521 (2007).
- Martins, E. R. et al. Deterministic quasi-random nanostructures for photon control. *Nat. Commun.* **4**, 2665 (2013).
- Ozaki, M., Kato, J.-i. & Kawata, S. Surface-plasmon holography with white-light illumination. *Science* **332**, 218–220 (2011).
- Zheng, G. et al. Metasurface holograms reaching 80% efficiency. *Nat. Nanotechnol.* **10**, 308–312 (2015).
- Tittl, A. et al. Imaging-based molecular barcoding with pixelated dielectric metasurfaces. *Science* **360**, 1105–1109 (2018).
- Mahler, L. et al. Quasi-periodic distributed feedback laser. *Nat. Photon.* **4**, 165–169 (2010).
- Yoshida, M. et al. Double-lattice photonic-crystal resonators enabling high-brightness semiconductor lasers with symmetric narrow-divergence beams. *Nat. Mater.* **18**, 121–128 (2019).
- Ayata, M. et al. High-speed plasmonic modulator in a single metal layer. *Science* **358**, 630–632 (2017).
- Lu, L., Joannopoulos, J. D. & Soljacic, M. Topological photonics. *Nat. Photon.* **8**, 821–829 (2014).
- Pendry, J. B., Huidobro, P. A., Luo, Y. & Galiffi, E. Compacted dimensions and singular plasmonic surfaces. *Science* **358**, 915–917 (2017).
- Hu, G. et al. Coherent steering of nonlinear chiral valley photons with a synthetic Au–WS₂ metasurface. *Nat. Photon.* **13**, 467–472 (2019).
- Genevet, P., Capasso, F., Aieta, F., Khorasaninejad, M. & Devlin, R. Recent advances in planar optics: from plasmonic to dielectric metasurfaces. *Optica* **4**, 139–152 (2017).
- Kim, J., Joy, D. C. & Lee, S. Y. Controlling resist thickness and etch depth for fabrication of 3D structures in electron-beam grayscale lithography. *Microelectron. Eng.* **84**, 2859–2864 (2007).
- Dakss, M. L., Kuhn, L., Heidrich, P. F. & Scott, B. A. Grating coupler for efficient excitation of optical guided waves in thin films. *Appl. Phys. Lett.* **16**, 523–525 (1970).
- Campbell, M., Sharp, D. N., Harrison, M. T., Denning, R. G. & Turberfield, A. J. Fabrication of photonic crystals for the visible spectrum by holographic lithography. *Nature* **404**, 53–56 (2000).
- Shi, L. et al. Spatial coherence properties of organic molecules coupled to plasmonic surface lattice resonances in the weak and strong coupling regimes. *Phys. Rev. Lett.* **112**, 153002 (2014).
- Kurvits, J. A., Jiang, M. & Zia, R. Comparative analysis of imaging configurations and objectives for Fourier microscopy. *J. Opt. Soc. Am. A* **32**, 2082–2092 (2015).
- Barnes, W. L., Preist, T. W., Kitson, S. C. & Sambles, J. R. Physical origin of photonic energy gaps in the propagation of surface plasmons on gratings. *Phys. Rev. B* **54**, 6227–6244 (1996).
- Joannopoulos, J. D., Johnson, S. G., Winn, J. N. & Meade, R. D. *Photonic Crystals: Molding the Flow of Light* (Princeton Univ. Press, 2008).
- Chao, W., Harteneck, B. D., Liddle, J. A., Anderson, E. H. & Attwood, D. T. Soft X-ray microscopy at a spatial resolution better than 15 nm. *Nature* **435**, 1210–1213 (2005).
- Wang, Y., Yun, W. & Jacobsen, C. Achromatic Fresnel optics for wideband extreme-ultraviolet and X-ray imaging. *Nature* **424**, 50–53 (2003).
- Di Fabrizio, E. et al. High-efficiency multilevel zone plates for keV X-rays. *Nature* **401**, 895–898 (1999).
- Vitiello, M. S. et al. Photonic quasi-crystal terahertz lasers. *Nat. Commun.* **5**, 5884 (2014).
- Huang, Z. Q., Marks, D. L. & Smith, D. R. Out-of-plane computer-generated multicolor waveguide holography. *Optica* **6**, 119–124 (2019).
- Yoo, D., Johnson, T. W., Cherukulappurath, S., Norris, D. J. & Oh, S. H. Template-stripped tunable plasmonic devices on stretchable and rollable substrates. *ACS Nano* **9**, 10647–10654 (2015).
- Wuttig, M., Bhaskaran, H. & Taubner, T. Phase-change materials for non-volatile photonic applications. *Nat. Photon.* **11**, 465–476 (2017).
- Shaltout, A. M., Shalae, V. M. & Brongersma, M. L. Spatiotemporal light control with active metasurfaces. *Science* **364**, eaat3100 (2019).
- Arbabi, A., Horie, Y., Bagheri, M. & Faraon, A. Dielectric metasurfaces for complete control of phase and polarization with subwavelength spatial resolution and high transmission. *Nat. Nanotechnol.* **10**, 937–943 (2015).
- Rubin, N. A., D'Aversa, G., Chevalier, P., Shi, Z., Chen, W. T. & Capasso, F. Matrix Fourier optics enables a compact full-Stokes polarization camera. *Science* **365**, eaax1839 (2019).

Publisher's note Springer Nature remains neutral with regard to jurisdictional claims in published maps and institutional affiliations.

© The Author(s), under exclusive licence to Springer Nature Limited 2020

Methods

Fourier-surface design

All surfaces were designed using analytical functions. In general, 1D real-space height profiles, $f(x)$, can be obtained from the desired Fourier spectrum, $F(K)$, via the 1D inverse Fourier transform:

$$f(x) = \frac{1}{2\pi} \int_{-\infty}^{\infty} F(K) e^{iKx} dK \quad (1)$$

K is a spatial-frequency variable and $F(K)$ describes the spatial frequencies (g) contained in the surface profile. Similarly, 2D height profiles, $f(x, y)$, follow from the 2D inverse Fourier transform of $F(K_x, K_y)$:

$$f(x, y) = \frac{1}{(2\pi)^2} \iint_{-\infty}^{\infty} F(K_x, K_y) e^{i(K_x x + K_y y)} dK_x dK_y \quad (2)$$

K_x and K_y are spatial-frequency variables along the x and y axes. For $f(x)$ and $f(x, y)$, the origin is placed in the middle of the pattern for both x and y . All functions are defined for the pattern in the polymer surface, where x and y lie in-plane and z is perpendicular. In these formulas, the height of the surface is defined relative to the unpatterned flat surface where $z = 0$. Note that the Fourier spectra in equations (1) and (2), used to calculate the infinitely extended real-space surface profiles, neglect finite-size effects. The finite dimensions of the experimental profile lead to broadening of the Fourier spectra (see Methods section 'Analytical model').

For the Fourier surfaces in Figs. 1 and 4 and Extended Data Figs. 1, 2, 4, 5, 6, 8 and 9, the Fourier spectrum is sufficiently simple (with one, two or three Fourier components, assuming infinite size in x, y) that the height profile can be written as a sum of sinusoids:

$$f(x) = \sum_i A_i \cos(g_i x + \varphi_i) - \Delta \quad (3)$$

where A_i , g_i and φ_i are the amplitude, spatial frequency, and phase, respectively, for component i . Note that in equation (3), the sinusoidal surface profiles in the polymer are vertically shifted in z by $-\Delta$. When templating is used to transfer the pattern to Ag, the surface profile is inverted and vertically shifted in z by $+\Delta$. For clarity, all parameters for our polymer surfaces are provided in Extended Data Table 1.

For the Fourier surfaces in Figs. 2a, b, 3a, d, 4e and Extended Data Figs. 7, 9, the height profile was given by:

$$f(x, y) = \sum_i A_i \cos[g_i (x \cos \theta_i + y \sin \theta_i) + \varphi_i] - \Delta \quad (4)$$

where θ_i is the in-plane rotation angle from the x axis for component i . The circular Fourier surfaces in Extended Data Fig. 7 follow:

$$f(r, \theta) = \sum_i A_i \cos(g_i |\mathbf{r} - \mathbf{r}_i| + \varphi_i) - \Delta \quad (5)$$

where r and θ are the radial distance and polar angle, respectively. \mathbf{r} is the coordinate in the surface plane and is a function of r and θ . \mathbf{r}_i is the centre of circular component i . The sinusoidal zone plate⁴² in Fig. 2e follows the function:

$$f(r) = A \sin \left[\pi \left(\frac{r}{L} \right)^2 \right] - \Delta \quad (6)$$

where A is an amplitude and L is a characteristic length.

Bitmap generation

The analytical functions defining the Fourier surfaces are converted into bitmaps. The overall dimensions in x and y are chosen for the

structure, and the analytical function is mapped onto a 10 nm \times 10 nm pixel grid. The normalized depth of the structure in z was assigned for each pixel by discretizing the total normalized depth to 256 levels (8-bit precision). The physical patterning depth was assigned for each pixel by inputting the maximum physical depth of the structure to the thermal scanning-probe control software (see Methods section 'Fourier-surface fabrication'), which then assigned the physical depth for each pixel based on its 8-bit depth level. The entire process flow, from analytical mathematical design to pattern transfer to an optical material, is depicted in Extended Data Fig. 1.

Materials

1-mm-thick glass microscope slides and 1-mm-thick, 2-inch-diameter and 4-inch-diameter Si(100) wafers (1–10 Ω cm resistivity) were purchased from Paul Marienfeld and Silicon Materials, respectively. Ag (1/4-inch-diameter \times 1/4-inch-long pellets, 99.999%), Au (1/8-inch-diameter \times 1/8-inch-long pellets, 99.999%), TiO₂ sputter targets (200 mm diameter, 99.95%), and ultraviolet-curable epoxy (OG142-95 and OG116-31) were obtained from Kurt J. Lesker, ACI Alloys, FHR Anlagenbau, and Epoxy Technology, respectively. Tungsten dimple boats (49 \times 12 \times 0.4 mm³) were bought from Umicore. Two polymer resists from Allresist GmbH were used: PMMA/MA [AR-P 617, poly(methyl methacrylate-co-methacrylic acid), 33% copolymer, 3% dilution in anisole] and CSAR [AR-P 6200, containing poly(α -methylstyrene-co-methyl chloroacrylate) in anisole]. For electron-beam lithography, the CSAR resist was developed using AR 600-546 from Allresist. Silicon cantilevers for thermal scanning-probe lithography with a tip radius of ~3–5 nm were provided by SwissLitho (SL2015-2-HPL, SL2016-3-HPL, SL2018-13-HPL and SL2018-2-MBS). Hydrochloric acid (HCl, 37%), nitric acid (HNO₃, \geq 65%), sulfuric acid (H₂SO₄, \geq 95%), and ammonium fluoride + hydrofluoric acid etching mixture (AF 875-125) were purchased from Sigma-Aldrich. Hydrogen peroxide (H₂O₂, 30%) was obtained from VWR Chemicals. Acetone and isopropanol (IPA) were provided by the Binnig and Rohrer Nanotechnology Center (BRNC) at IBM Zurich, where the templates were fabricated.

Fourier-surface fabrication

A Si wafer was typically used as the sample substrate. It was removed from its factory packaging in the cleanroom and used directly. The polymer resist layer was spin-coated onto it using a two-step procedure. For PMMA/MA or CSAR, the resist solution was deposited on the sample surface and accelerated at 500 rpm s⁻¹ to 500 rpm for 5 s. Then the PMMA/MA (CSAR) was accelerated at 2,000 rpm s⁻¹ to 2,000 rpm (2,500 rpm) for a total time of 40 s. After spin-coating, the PMMA/MA (CSAR) layer was baked at 180 $^{\circ}$ C for 5 min (150 $^{\circ}$ C for 1 min). For the deeper Fourier surface structures in Extended Data Fig. 8, the PMMA/MA spin-coating and baking procedure was repeated to double the thickness of the resist layer from ~150 nm to ~300 nm.

For thermal scanning-probe lithography, the substrate/polymer stack was placed in a NanoFrazor Explore (SwissLitho). A cantilever with a sharp tip was loaded into the cantilever holder, which was then attached to the NanoFrazor scan head. The tip was brought close to the sample and an auto-approach function achieved surface contact. The tip position, temperature response and sample tilt were calibrated. The temperature at the base of the tip was set to an initial value between 700 $^{\circ}$ C and 950 $^{\circ}$ C, depending on the cantilever model. Calibration scans were performed to optimize the patterning depth of the sinusoidal structures. The bitmap defining the desired Fourier surface was then loaded into the NanoFrazor software. The tip was scanned across the patterning surface on a 10 nm \times 10 nm pixel grid. A force pulse (~6 μ s) was applied at each pixel to match the depth level of the bitmap in the polymer resist. As the tip patterned the surface, it simultaneously measured the topography as in contact-mode atomic force microscopy (AFM). The measured error between the written pattern and the desired pattern was passed to a feedback loop such that the write

force could be adjusted to reach the desired depth level, if necessary. The scan progressed until all pixels in the design were patterned into the surface, at which point the tip was available to write the next pattern.

To obtain Ag diffractive surfaces, Ag was thermally evaporated⁴³ (Kurt J. Lesker, Nano36) onto the patterned polymer film at a pressure of about 3×10^{-7} mbar. A tungsten boat loaded with Ag pellets was heated to deposit at a rate of 25 \AA s^{-1} . The process was stopped when the film thickness was around 750 nm. A glass slide was then affixed with ultraviolet-curable epoxy (OG142-95) onto the exposed Ag surface, and the glass/epoxy/Ag stack peeled off, revealing a Ag surface with the negative of the initial pattern in the polymer surface.

SiN_x surfaces were obtained by using a $\text{Si}/\text{SiO}_2/\text{SiN}_x$ stack as a substrate. A layer of SiO_2 , 2,000 nm thick was thermally grown onto a Si wafer, followed by chemical vapour deposition of a layer of SiN_x , 200 nm thick. The wafer was diced into $1.5 \text{ cm} \times 1.5 \text{ cm}$ pieces for thermal scanning-probe lithography using PMMA/MA as the polymer. The pattern in the polymer film was transferred into the underlying SiN_x substrate via reactive-ion etching (Oxford Instruments, NPG 80) using a gas mixture of 50 standard cubic centimetres per minute (sccm) CHF_3 and 5 sccm O_2 . The etching was performed at a chamber pressure of 55 mTorr, with 100 W radio-frequency power and a SiN_x etch rate of 45 nm min^{-1} for 5 min, where the depth of the transferred pattern in SiN_x was approximately the same as the depth in the polymer pattern (approximately 1:1 selectivity). Afterwards, the substrate was ultrasonicated in acetone, followed by isopropanol, and blown dry with N_2 .

To obtain Si surfaces for either direct use or for templating, the pattern in the polymer film was transferred into the underlying Si substrate via inductively coupled plasma etching (Oxford Instruments, Plasma Pro) using a gas mixture of 17.0 sccm SF_6 , 17.5 sccm C_4F_8 and 60 sccm Ar. The Si etching was done at a chamber pressure of 20 mTorr, with a forward power of 50 W, and at a rate of $\sim 25 \text{ nm min}^{-1}$ for 6.33 min, where the depth of the transferred pattern in Si was approximately the same as the depth in the polymer pattern (approximately 1:1 selectivity). After etching, the sample was sonicated for 2 min in acetone and 2 min in IPA, followed by 5 min of O_2 plasma cleaning at 600 W.

Patterned TiO_2 samples were obtained by using patterned Si templates. A 25-nm-thick Au layer was thermally evaporated onto the patterned Si wafer at a pressure of approximately 3×10^{-7} mbar and a rate of 10 \AA s^{-1} . TiO_2 was then radio-frequency-sputtered onto the exposed gold surface (von Ardenne, CS 320 S) with 400 W, a chamber pressure of 4×10^{-3} mbar, and 14 sccm Ar, for 160 min, resulting in an approximately 300-nm-thick film. A glass slide was then affixed with ultraviolet-curable epoxy (OG116-31) onto the exposed TiO_2 layer, and the glass/epoxy/ TiO_2 /Au stack peeled off, revealing a TiO_2 /Au surface with the negative of the initial pattern in the Si surface. Finally, the Au layer was removed by immersing the sample in aqua regia (4:1 mixture of $\text{HCl}:\text{HNO}_3$) for 5 min. Afterwards, the sample was rinsed in deionized water and blown dry with N_2 .

Binarized-surface design and fabrication

For each Fourier surface in Fig. 1 with height profile $f(x)$ (see Extended Data Table 1), a binarized version was fabricated by electron-beam lithography and etching, followed by templating (see Extended Data Fig. 4). The binarization followed a published thresholding procedure⁴⁴. This required the electron-beam lithography resist to be exposed wherever $f(x) + \Delta < 0$. The Si substrate was then etched in these locations.

To prepare the samples, $2 \times 2 \text{ cm}$ chips (diced from a 4-inch-diameter, 1-mm-thick Si wafer) were cleaned by sonicating for 2 min in acetone and 2 min in IPA, followed by 5 min of O_2 plasma cleaning at 600 W. CSAR (electron-beam lithography resist) was deposited on the sample surfaces and accelerated at 500 rpm s^{-1} to 500 rpm for 5 s in a first spin-coating step. In a second step, the samples were accelerated at $2,000 \text{ rpm s}^{-1}$ to 2,000 rpm for a total time of 40 s. After spin-coating, the samples were baked at $150 \text{ }^\circ\text{C}$ for 1 min. The samples were then

loaded into an electron-beam lithography system (Vistec, NFL 5) and patterned by exposing the resist layer where specified by the thresholding procedure⁴⁴. After exposure, the samples were developed in AR 600-546 for 1 min, and subsequently rinsed in IPA. The patterns were etched to depths approximately matching that of the corresponding Fourier surfaces from Fig. 1 with HBr-based reactive-ion etching (Oxford, Plasmalab System 100). The Si etching was done using 40 sccm HBr at a chamber pressure of 3 mTorr, with a forward power of 200 W, radio-frequency power of 20 W, and at a rate of approximately 30 nm min^{-1} for 2 min. After etching, the resist was removed by subsequent sonication in acetone and in IPA, followed by 2 min of O_2 plasma cleaning at 600 W, a dip in buffered hydrofluoric acid (1:7 mixture of AF 875-125 and H_2O), and rinsing with H_2O . The samples were cleaned in piranha (1:1 mixture of $\text{H}_2\text{SO}_4:\text{H}_2\text{O}_2$) for 15 min, ultrasonicated in H_2O and in IPA, and blown dry with N_2 . (Caution: care should be taken with piranha as it reacts violently with solvents and other organic materials.) These binarized surfaces were then replicated in Ag using the same procedure as for the Fourier surfaces.

Surface-topography characterization

The topography of the Fourier surfaces was measured by the scanning probe during patterning and independently verified with AFM on the templated Ag surface. The topography of our Ag single-sinusoidal surface (Fig. 1a, b) is analysed in Extended Data Fig. 2. AFM scans (Bruker, Dimension FastScan AFM with a Bruker NCHV-A cantilever) were collected in tapping mode under ambient conditions. The raw data was processed by first removing the instrumental high-frequency scan noise in the scanning-probe analysis software Gwyddion (version 2.54, <http://gwyddion.net>). Next, row alignment and plane-levelling were performed in MATLAB (version 2019a, <http://ch.mathworks.com/products/matlab.html>) to obtain the corrected data, shown in Extended Data Fig. 2a. These data were then analysed by fitting a sinusoidal function (with the form shown in Extended Data Table 1 for Fig. 1a; periodic along x , constant in y), where the fit parameters and residuals were extracted. The amplitude and period of the fitted function were $A_1 = 25.5 \text{ nm}$ (2% larger than design value) and $\Lambda = 610 \text{ nm}$ (1.7% larger than design value), respectively. As we obtained a consistent horizontal distance error in both our etched and templated gratings, we attributed this error to a distance miscalibration in the thermal scanning probe. The RMS error between the design function and measured topography for the structure in Fig. 1a was found to be 1.8 nm after this error was taken into account. A similar procedure was used to extract RMS errors for other Fourier surfaces, as reported in the legends of Fig. 1 and Extended Data Fig. 9. See Extended Data Fig. 2 for further details. For the photonic diffraction gratings in Extended Data Fig. 8, a slight nonlinearity in the patterning of deeper structures was also taken into account.

Optical characterization

The optical-characterization setup is depicted in Extended Data Fig. 3a. Ag surfaces were measured with an inverted optical microscope (Nikon, Eclipse Ti-U) equipped with a $50\times$ air objective (Nikon, TU Plan Fluor, numerical aperture $\text{NA} = 0.8$). A halogen lamp was used to illuminate the sample. The lamp filament was imaged onto the back focal plane of the microscope objective. After a beamsplitter, the light was focused onto the sample and then collected by the same objective. Reflected light was transmitted through the beamsplitter and passed through a circular aperture in the real-space image plane to isolate the structure of interest. The back focal plane was imaged onto the entrance slit of an imaging spectrograph (Andor Shamrock 303i) where it was relayed to a sensitive digital camera (Andor Zyla PLUS sCMOS) for image acquisition. Reflectivity measurements were obtained for both dispersed k -space measurements (Fig. 1c, f, i, Extended Data Fig. 4b, d, f, Extended Data Fig. 5b and Extended Data Fig. 6b–i) and k -space images (Fig. 2c, d and Fig. 3c, f), by acquiring a background image, a reference image and a signal image. The background, reference and signal images were

recorded by acquiring the counts when no light was incident on the camera, when light was reflected from flat Ag on the sample and when light was reflected from the pattern of interest, respectively. The final reflectivity image was calculated using:

$$\text{Reflectivity (\%)} = 100 \times (\text{Signal} - \text{Background}) / (\text{Reference} - \text{Background}) \quad (7)$$

For the dispersed k -space measurements, a grating (150 lines mm^{-1} blazed at 500 nm) was inserted into the imaging path in the spectrometer such that the light was spectrally dispersed along one axis of the camera. The spectrometer slit was parallel to k_x . A linear polarizer was inserted into the collection path to select only p-polarized light, which couples to SPPs. Thus, in a single acquisition, the dispersion relation (energy versus in-plane momentum along the surface modulation, k_x , with $k_y \approx 0$) could be measured. The experimental window is overlaid with a schematic of the theoretical SPP dispersion in Extended Data Fig. 3b.

For the k -space images, a bandpass filter centred at 570 nm with a full-width at half-maximum (FWHM) of 10 nm was placed in the excitation path. The linear polarizer was removed from the detection path such that the measurement collected all polarizations equally. The slit at the entrance of the imaging spectrograph was opened completely and the k -space image was relayed to the camera using a mirror instead of a diffraction grating to eliminate stray diffracted light. A schematic of this measurement, performed at a narrow range of photon energies selected by the bandpass filter, is depicted in Extended Data Fig. 3d. A cartoon of the complete light cone and SPP dispersion is depicted in Extended Data Fig. 3c.

The reflectivity spectrum in Fig. 4d was obtained by plotting the dispersed k -space measurement for the three-component Fourier surface in Fig. 4b at a fixed angle of incidence (near normal incidence). Spectra were averaged over a collection angle of $\pm 0.25^\circ$.

Analytical model

Optical modes bound to a periodic surface have an electric-field profile of the form

$$\mathbf{E}_{\mathbf{k}}(\mathbf{r}) = e^{-i\mathbf{k}\cdot\mathbf{r}} \mathbf{u}_{\mathbf{k}}(\mathbf{r}) \quad (8)$$

where \mathbf{k} is the Bloch wavevector of the mode, and $\mathbf{u}_{\mathbf{k}}(\mathbf{r})$ is a function with the same periodicity as the surface. We consider a grating profile with modulation in one dimension, like those in Fig. 1, for which all surface Fourier components i have an in-plane wavevector $\mathbf{g}_i = g_i \hat{\mathbf{x}}$. The overall periodicity $2\pi/G$ of the surface profile can be much longer than any of the periodicities $\{2\pi/g_1, 2\pi/g_2, \dots, 2\pi/g_N\}$ of the N constituent sinusoids:

$$G^{-1} = \text{LCM}(g_1^{-1}, g_2^{-1}, \dots, g_N^{-1}) \quad (9)$$

where LCM denotes the least common multiple. For example, the grating in Fig. 1g has an overall design periodicity of $2\pi/G = 96.6 \mu\text{m}$ and $G = 0.0650 \mu\text{m}^{-1}$. The full field profile of a mode $\mathbf{E}_{\mathbf{k}}(\mathbf{r})$ contains all in-plane wavevector components $(k_x + nG, k_y)$ with any integer n . However, to calculate the plasmonic dispersion and stopbands of our Fourier surfaces in Fig. 1, we do not need the full field profile. Instead, we can use a relatively simple coupled-mode model with a limited basis, which only accounts for first-order coupling between plane waves differing in wavevector by \mathbf{g}_i of one of the sinusoids of the grating.

On a flat Ag-dielectric interface, SPP modes have in-plane wavevector \mathbf{k}_{SPP} with magnitude:

$$k_{\text{SPP}} = \frac{\omega}{c} \sqrt{\frac{\varepsilon_m(\omega)\varepsilon_d}{\varepsilon_m(\omega) + \varepsilon_d}} \quad (10)$$

where ω is the SPP angular frequency, c is the speed of light in vacuum and ε_m is the frequency-dependent relative permittivity of the metal. The relative permittivity of the dielectric ε_d is assumed to be frequency-independent. We note that when calculating \mathbf{k}_{SPP} for Figs. 2, 3, we used $\varepsilon_d = 1.061$. This value was determined by fitting the SPP dispersion for an independent sample. Extracting a relative permittivity slightly above 1 was perhaps due to residual polymer on the Ag surface after templating. For the structures in Fig. 1, our fabrication process had been improved and $\varepsilon_d = 1$ was extracted and used for modelling.

In Fig. 1, we measure the dispersion of our Fourier surfaces along the k_x direction. Stopbands in this direction arise whenever $2k_{\text{SPP}} = g_i$ for one of the sinusoids i in the grating. This occurs at energies:

$$\hbar\omega_i = \frac{hc}{2n_{\text{eff}}\Lambda_i} \quad (11)$$

where $\hbar = h/(2\pi)$ with h as Planck's constant, and $n_{\text{eff}} = \sqrt{\varepsilon_m(\omega)\varepsilon_d/[\varepsilon_m(\omega) + \varepsilon_d]}$ is the effective refractive index of the SPP mode on the flat Ag-dielectric interface. Although the SPP dispersion, and any stopbands therein, lie outside the light cone, we can measure a stopband if some sinusoid j provides momentum to couple free-space photons to SPPs. The stopband will then appear in our reflectivity measurement at a photon in-plane wavevector with magnitude:

$$k_{ij} = n_{\text{eff}} \frac{\omega_i}{c} - g_j = 2\pi \left(\frac{1}{2\Lambda_i} - \frac{1}{\Lambda_j} \right) \quad (12)$$

To calculate the stopbands and the SPP dispersion for our Fourier surfaces more rigorously, we use a coupled-mode model. We couple SPPs—surface waves with wavevector component $k_{x,0} = k_{\text{SPP}}$ —to surface waves with $k_{x,i} = k_{\text{SPP}} - g_i$ for all sinusoids $i \in \{1, 2, \dots, N\}$ in the surface profile. The coupling can be described by an interaction matrix H , which has dimensions $(N+1) \times (N+1)$. The diagonal elements of the matrix are the energies that a surface wave of wavevector component $k_{x,i}$ would have on a flat Ag-dielectric interface. We obtain these energies by evaluating the inverse of equation (10), $\omega(k_{\text{SPP}})$, at $k_{\text{SPP}} = |k_{x,i}|$:

$$H_{ii} = \hbar\omega(|k_{x,i}|) \quad (13)$$

For this, we use the relative permittivity data $\varepsilon_m(\omega)$ of template-stripped Ag (ref. 43) and $\varepsilon_d = 1$ for air. The off-diagonal elements of the matrix, H_{ij} , describe the interaction between surface waves i and j . For simplicity, we consider only coupling involving the SPP wave, which has a wavevector component $k_{x,0} = k_{\text{SPP}}$, and neglect coupling between surface waves with $i \geq 1$ and $j \geq 1$. Thus, the only non-zero off-diagonal elements of H are:

$$H_{0i} = H_{i0} = \hbar\Gamma_i \quad (14)$$

Here Γ_i is the (real-valued) rate at which the surface sinusoid i of the surface profile couples a surface wave with $k_{x,0}$ (that is, the SPP on a flat Ag-air interface) to a surface wave with $k_{x,i}$. This rate determines the width of the stopband $\Delta E_i \approx 2\hbar\Gamma_i$ owing to the grating component i . Extended Data Fig. 6 shows that we can control this by tuning the corresponding amplitude A_i of the sinusoid³⁰. For Fig. 1i, we estimated values of Γ_i based on the dispersion data and plugged them into the model.

By solving for the eigenvalues of H , we obtain the energies E_i of the coupled modes. The eigenvectors \mathbf{v}_i describe their composition in terms of the surface-wave basis functions. For each coupled mode, the first component of the eigenvector $v_{i,0}$ represents its SPP character.

So far, we have treated the coupling matrix H for a single value of k_{SPP} . However, to calculate dispersion plots such as those in Fig. 1, we must determine the eigenvalues and eigenvectors of H for a range of k_{SPP} . Thus, we considered a series of k_{SPP} values, labelled by $m \in \{1, 2, \dots, M\}$, from 0 and $25 \mu\text{m}^{-1}$ in $M = 5,001$ steps of $0.005 \mu\text{m}^{-1}$. At each $k_{\text{SPP},m}$, the

corresponding coupling matrix H_m yields a set of $(N + 1)$ mode energies $E_{m,i}$ and $(N + 1)$ values $v_{m,i,0}$ for their corresponding SPP character (the coefficient for the contribution of the SPP with $k_{x,0} = k_{\text{SPP},m}$ to the eigenvector of coupled mode j).

Now, in addition to coupling surface waves, we must include the fact that each sinusoid l in the surface profile ($l \in \{1, 2, \dots, N\}$) can enable free-space photons to excite SPPs if $|k_{\text{SPP}} - g_l| \leq \omega/c$ (that is, if the in-plane momentum required from the photon is inside the light cone). Free-space photons with in-plane wavevector $\mathbf{k}_{\parallel} = (k_x, 0)$ can excite SPPs if the momentum from sinusoid l matches coupled mode i with substantial SPP character $v_{i,0}$. We account for photon–SPP momentum-matching by considering the effect of grating components l again only in first order. Starting with the dispersion calculated in the last paragraph ($N + 1$ energies $E_{m,i}$ at each $k_{\text{SPP},m}$), we generate N copies of this dispersion by shifting the wavevector value to $k_{m,l} = k_{\text{SPP},m} - g_l$ for all $l \in \{1, 2, \dots, N\}$. These $k_{m,l}$ are the k values for which grating component l can in principle enable SPP incoupling. Then we copy and mirror the entire dispersion in the ($k = 0$) axis, realizing that the entire problem is symmetric under inversion of the propagation direction of the modes. We thus obtain $2N$ copies of our calculated dispersion, some of which may fall entirely outside the experimental range of wavevectors and energies. We consider that at each point $(k_{m,l}, E_{m,i})$ or $(-k_{m,l}, E_{m,i})$, with $m \in \{1, 2, \dots, M\}$, $i \in \{0, 1, 2, \dots, N\}$ and $l \in \{0, 1, 2, \dots, N\}$, the coupling to SPPs is proportional to $\Gamma_l v_{m,i,0}^2$. This reflects that, for first-order coupling, the magnitude of the admixture is proportional to the SPP character of the coupled mode. We thus obtain a model function for the incoupling V as a function of the photon in-plane wavevector component k_x and energy $\hbar\omega$ of:

$$V(k_x, \hbar\omega) = \sum_{m=1}^M \sum_{i=0}^N \sum_{l=0}^N \Gamma_l v_{m,i,0}^2 \delta(k_x \pm k_{m,l}) \delta(\hbar\omega - E_{m,i}) \quad (15)$$

where δ is the Kronecker delta function. Finally, we broaden V by convolution with a function:

$$P(k_x) = \text{sinc}^2(k_x d / 2) \quad (16)$$

in the k_x direction that accounts for the finite length $d = 9 \mu\text{m}$ of our gratings. We also convolute V with a Gaussian function $Q(\hbar\omega)$ with a variance of $\sigma^2 = (15 \text{ meV})^2$ in the $\hbar\omega$ direction to match the experimental broadening. This arises from a combination of finite instrumental resolution, losses and the finite range of k_y values for reflected photons. The convolved function $(V * P * Q)(k_x, \hbar\omega)$ is plotted in Fig. 1c, f, i.

Quantification of diffraction efficiencies

We experimentally quantify the diffraction efficiencies of Fourier surfaces (Extended Data Fig. 8) with an optical k -space excitation and imaging setup. We illuminate the sample with monochromatic light at normal incidence and quantify the fraction of light that is diffracted and leaves the sample at off-normal angles. Light from a supercontinuum laser source (NKT, Fianium, repetition rate 7.8 MHz) was filtered to a linewidth of about 1 nm using a tunable filter box (NKT, LLTF Contrast) and was collimated after the output of a single-mode fibre using an objective (Nikon, TU Plan Fluor 10 \times , NA 0.3). After passing through a 750-nm short-pass filter, a fraction of the beam was directed to a power meter using a beam splitter. The remaining beam was sent through a reflective neutral-density filter and a linear polarizer (polarization direction, s or p, as specified in Extended Data Fig. 8) before being focused onto the centre of the back focal plane of a microscope objective (Nikon, TU Plan Fluor 50 \times , NA 0.8) using a lens with focal length $f = 750 \text{ nm}$ (placed a distance f before the back focal plane). In this optical configuration the sample of interest in the focus of the microscope objective was illuminated with light from a narrow set of solid

angles centred around normal incidence. The finite size of the focused laser beam on the back focal plane resulted in a defocused Gaussian illumination spot on the investigated sample. The light reflected and diffracted by the sample was collected through the same microscope objective, redirected with a beam splitter and used to image the back focal plane of the microscope objective onto a sensitive digital camera (Andor, Zyla PLUS sCMOS). A real-space aperture in the relay system of the collection path was reduced to a diameter comparable to the side length of the Fourier surface. In this optical configuration, the illumination wavelength λ was varied between 450 nm and 700 nm in steps of 1 nm while recording one back focal plane image per wavelength step with 5 ms acquisition time. This process was done subsequently for the Fourier surface under investigation and for flat Ag as a reference. A separate image without laser illumination was subtracted from each k -space image to remove the background counts of the detector. The k -space images were subsequently corrected for power fluctuations of the supercontinuum source (as measured with the power meter), resulting in two sets of k -space images for the investigated Fourier surface and the flat Ag reference, respectively. The k -space images of the reference sample showed a bright spot centred around $k_x = k_y = 0$ with summed intensity $I_{\text{ref}}(\lambda)$, corresponding to specular reflection of the beam impinging on and exiting from the flat reference surface at normal incidence. For Fourier surfaces periodic along the x direction additional spots were observed centred around $k_x = g_i$, $k_y = 0$ with $i = \pm 1$. The intensity of each spot $I_i(\lambda)$ was extracted by summing the corresponding pixels of the k -space images. The diffraction efficiencies were calculated as $\eta_i(\lambda) = I_i(\lambda)/I_{\text{ref}}(\lambda)$, corresponding to the fraction of impinging photons diffracted into diffraction order i . We note that this formula neglects reflection losses from flat Ag (a few per cent).

Data availability

The data supporting the findings of this study are available from the corresponding author on reasonable request.

42. Moreno, V., Román, J. F. & Salgueiro, J. R. High efficiency diffractive lenses: deduction of kinoform profile. *Am. J. Phys.* **65**, 556–562 (1997).
43. McPeak, K. M. et al. Plasmonic films can easily be better: rules and recipes. *ACS Photonics* **2**, 326–333 (2015).
44. Kapsalidis, F. et al. Dual-wavelength DFB quantum cascade lasers: sources for multi-species trace gas spectroscopy. *Appl. Phys. B* **124**, 107 (2018).

Acknowledgements We thank S. Bonanni, U. Drechsler, F. Enz, T. Kulmala, A. Olziersky and R. Stutz for technical assistance and D. Chelladurai, U. Dürig, R. Keitel, A. Knoll, M. Kohli, N. Rotenberg, D. Thureja, J. Winkler and H. Wolf for discussions. This project was funded by the European Research Council under the European Union's Seventh Framework Program (FP/2007-2013)/ERC Grant Agreement Number 339905 (QuaDoPS Advanced Grant). F.T.R. (Rubicon-680-50-1509, Gravitation Program “Multiscale Catalytic Energy Conversion”, Veni-722.017.002), S.J.W.V. (OCENW.KLEIN.008) and B.I.F. (Rubicon-680-50-1513) acknowledge support from the Netherlands Organisation for Scientific Research.

Author contributions N.L., B.I.F. and D.J.N. conceived the project. N.L., R.B. and S.J.W.V. designed the Fourier surfaces with input from K.R., F.T.R. and D.J.N. N.L. patterned the polymer surfaces with assistance from K.R., M.S. and S.B. N.L. and R.B. transferred the patterns to optical materials with assistance from K.R. and M.S. N.L. performed the characterization and topography analysis of the Fourier surface structures. N.L. and R.B. performed the optical experiments. N.L., R.B., S.J.W.V. and F.T.R. analysed the optical data. F.T.R. developed the analytical model. N.L. and D.J.N. wrote the manuscript with input from all authors. D.J.N. supervised the project.

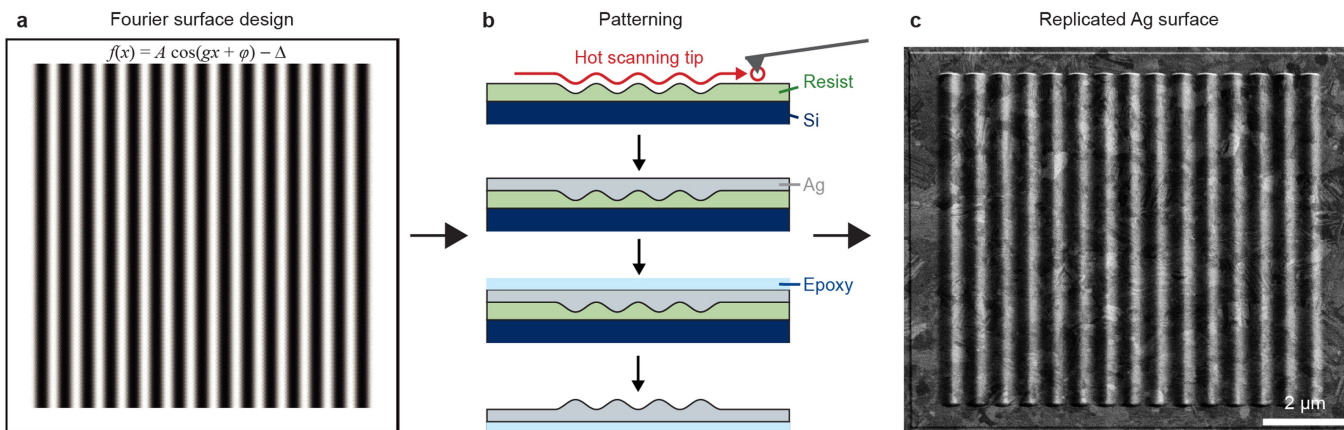
Competing interests The authors declare the following potential competing financial interests: S.B. is employed by Heidelberg Instruments Nano (previously SwissLitho AG), a provider of thermal scanning-probe lithography tools. At the time of his contribution, M.S. worked for SwissLitho AG. N.L., R.B., F.T.R. and D.J.N. have filed a patent application related to ideas in this work.

Additional information

Correspondence and requests for materials should be addressed to D.J.N.

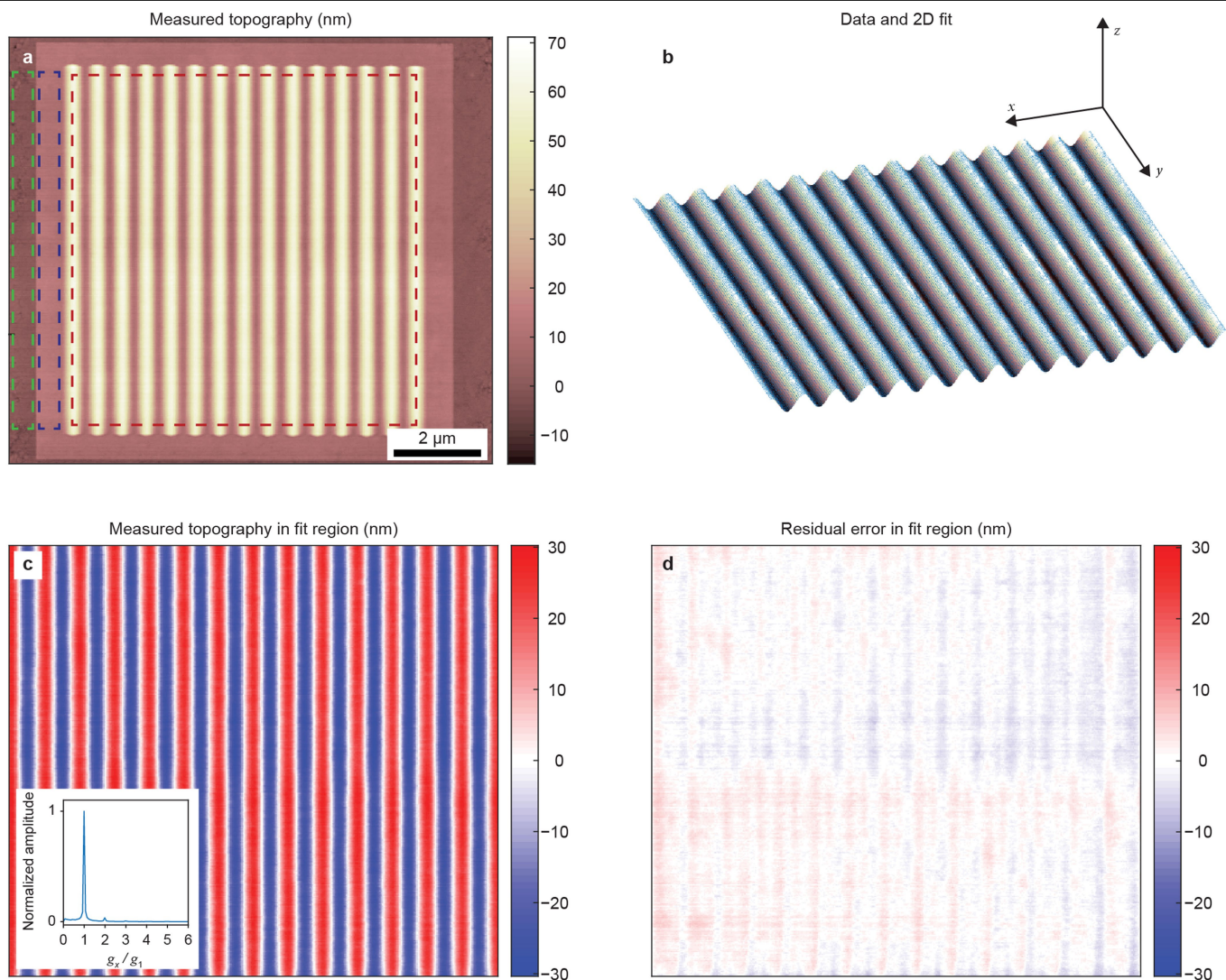
Peer review information *Nature* thanks Wei-Ting Chen, Maryna Meretska and the other, anonymous, and reviewer(s) for their contribution to the peer review of this work.

Reprints and permissions information is available at <http://www.nature.com/reprints>.



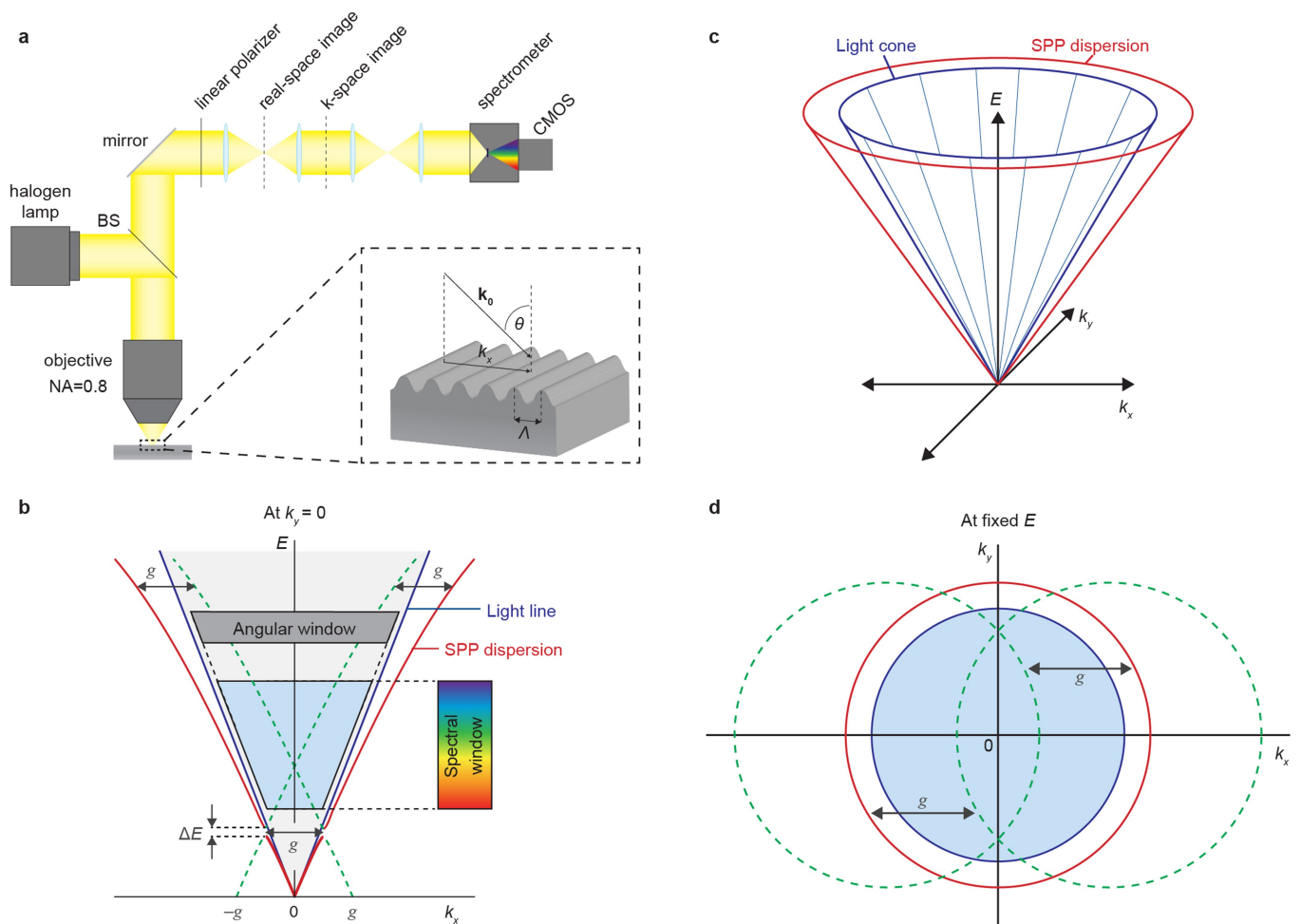
Extended Data Fig. 1 | Design and fabrication of Fourier surfaces. **a**, Design of a Fourier surface. The analytical formula for the desired surface profile (here, a single sinusoid modulated in 1D) is converted into a grayscale bitmap. Each $10 \text{ nm} \times 10 \text{ nm}$ pixel has a depth level between 0 and 255 (8-bit). The bitmap contains the sinusoidal function in the horizontal direction within the white border, which is constant along the vertical direction. The pixels in the white border are set to the minimum depth level. **b**, Process flow showing the patterning steps for Ag Fourier surfaces: (i) The hot scanning tip is used to

create a single sinusoid in the polymer resist, (ii) an optically thick ($>500 \text{ nm}$) Ag layer is thermally evaporated onto the polymer, (iii) a glass microscope slide is affixed to the back of the Ag layer using ultraviolet-curable epoxy, and (iv) the glass/epoxy/Ag stack is stripped off the polymer film. Alternative fabrication pathways for transferring the Fourier surface pattern to other materials are presented in the Methods. **c**, SEM (30° tilt) of a single-component Fourier surface transferred to Ag via templating. The initial analytical design is replicated accurately in the final Ag surface.



Extended Data Fig. 2 | Topography characterization. **a**, AFM micrograph of the measured topography (colour scale) for a single-sinusoidal Ag grating. The RMS roughness of the unpatterned flat Ag film is 1.6 nm, extracted from the area indicated by the green dashed box. The RMS roughness of the patterned flat Ag film is 1.3 nm, extracted from the area indicated by the blue dashed box. The area indicated by the red dashed box is used for fitting and analysis of the surface profile. **b**, 2D fit of a sinusoidal function (yellow/brown surface) to topography data (blue dots) from the region indicated in the red dashed box in **a**. The amplitude of the fitted function is $A_1 = 25.5$ nm (2% larger than design value) with a period of $\Lambda = 610$ nm (1.7% larger than design value). Such horizontal errors were consistent over many samples and attributed to a distance miscalibration in the thermal scanning probe. The RMS error between

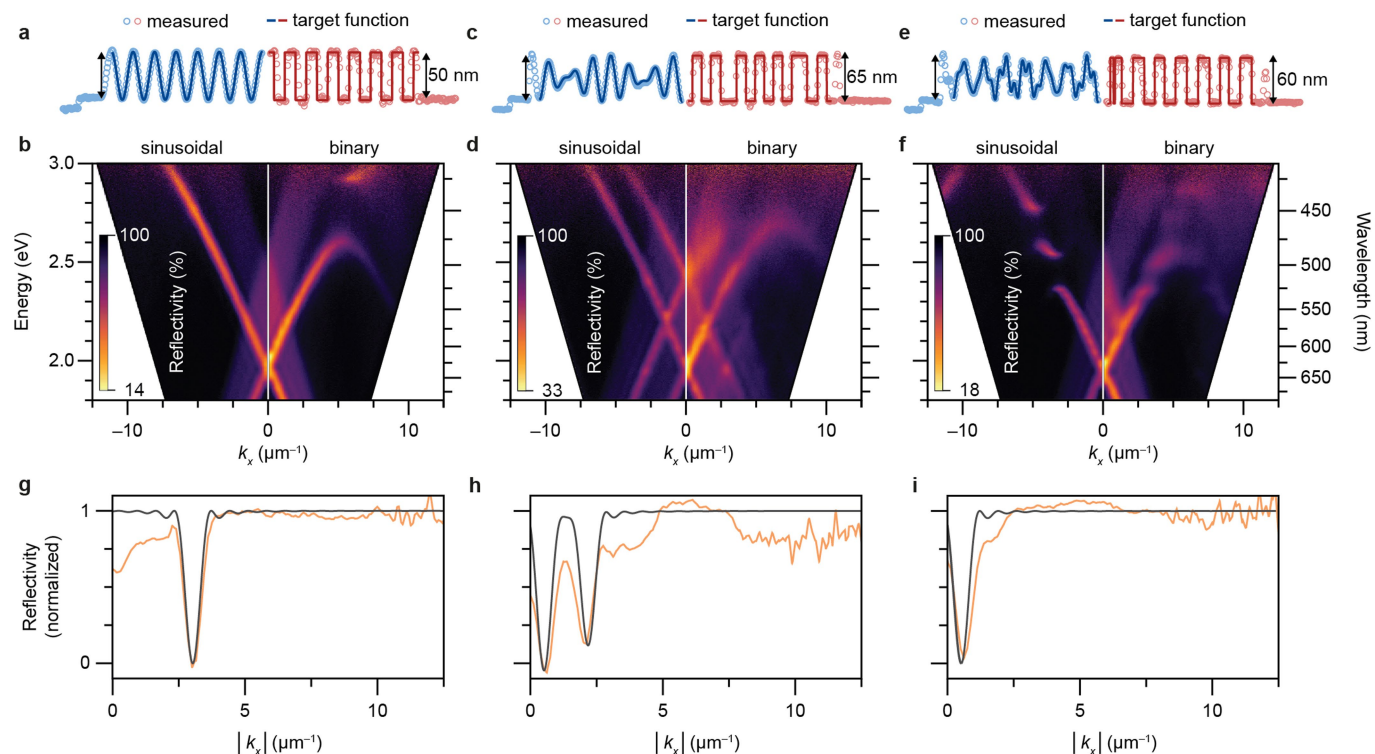
the design function and measured topography was found to be 1.8 nm after this horizontal error was taken into account. **c**, Measured topography (colour scale) of the structure in **a**, plotted only for the fit region (red dashed box in **a**), scaled from the minimum depth value to the maximum depth value and centred at zero. The inset shows a line cut (along g_x , at $g_y = 0$, where g_x and g_y are the components of \mathbf{g} along the x and y axes, respectively) from the 2D Fourier transform of the measured topography in the fit region, normalized to the peak value at g_1 . The second harmonic at $g_x/g_1 = 2$ is barely visible and has an amplitude of 3.5% of the peak at $g_x/g_1 = 1$, corresponding to a real-space amplitude of 0.9 nm. **d**, Residual error (colour scale) between the data and the fitted function, plotted for the fit region as in **c**. For comparison, the data are scaled over the same range as in **c**, centred at 0.



Extended Data Fig. 3 | Optical measurement of plasmonic Fourier surfaces.

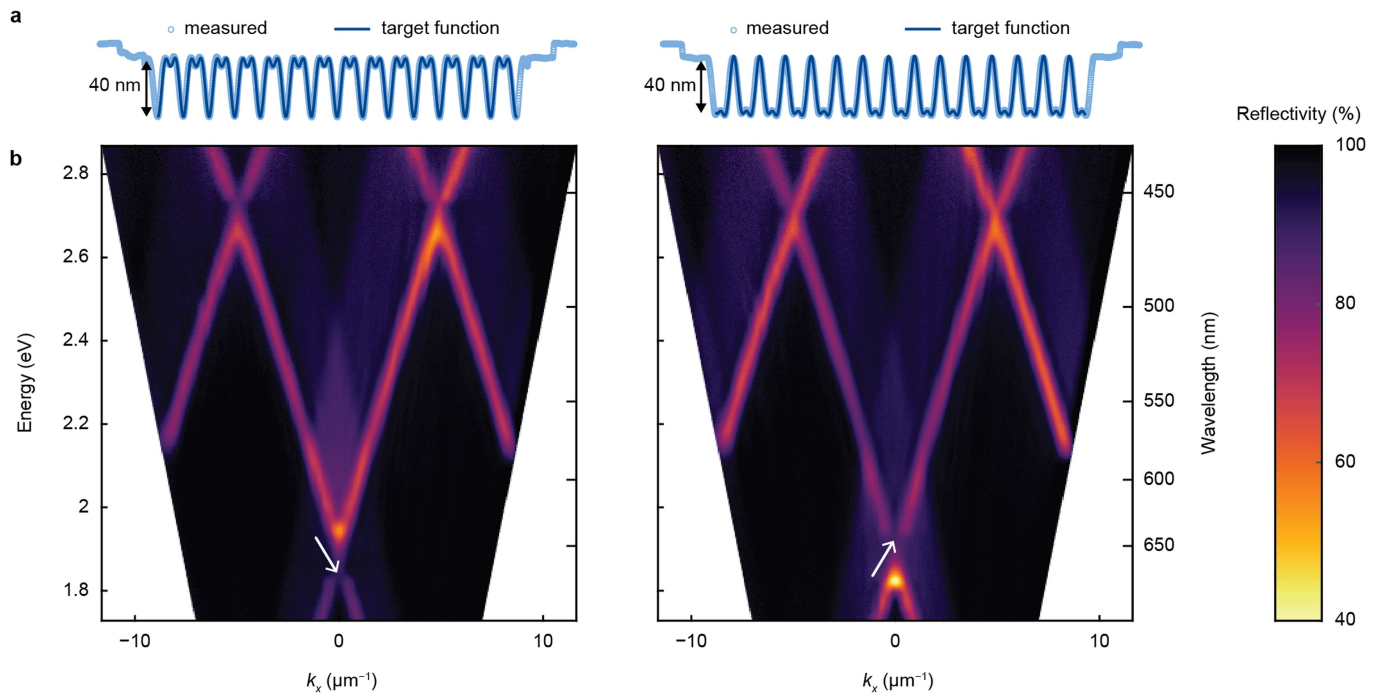
a, Schematic of the optical setup used for k -space reflectivity measurements. Further details are in the Methods. The inset shows a vector diagram of light with wavevector \mathbf{k}_0 incident at angle θ on a Fourier surface pattern with period Λ . BS, beamsplitter. CMOS, complementary metal-oxide-semiconductor digital camera. **b**, Schematic of the dispersion diagram (energy versus in-plane wavevector component, k_x) for free-space photons incident on a sinusoidal grating with $k_y = 0$ (as in Fig. 1). By tuning θ , photons have access to the shaded region inside the light lines (solid blue lines). The red lines show the SPP dispersion, k_{SPP} . Dashed green curves indicate the SPP dispersion displaced by the grating spatial frequency g . Inside the light line, these curves represent where free-space photons can couple to SPPs, and vice versa (that is, where

$k_x \pm g = k_{\text{SPP}}$). A stopband of width ΔE opens when counter-propagating SPPs are coupled by g . The blue trapezoidal region depicts the experimentally accessible area on the dispersion diagram, limited by the spectral window of the spectrometer along E , and the angular window of reflected light collected by the microscope objective along k_x . **c**, Schematic of the dispersion diagram for free-space photons incident on a surface, plotted for both in-plane wavevectors, k_x and k_y . The light line and SPP dispersion in **b** are both cones (blue and red lines, respectively). **d**, A slice through the dispersion diagram in **c** at fixed energy. Free-space photons incident on a surface can have wavevectors inside the light cone (blue-shaded region). The SPP dispersion is the larger red circle. Dashed green circles show solutions to $\mathbf{k}_i \pm \mathbf{g} = \mathbf{k}_{\text{SPP}}$. In this example, $\mathbf{g} = g\hat{x}$.



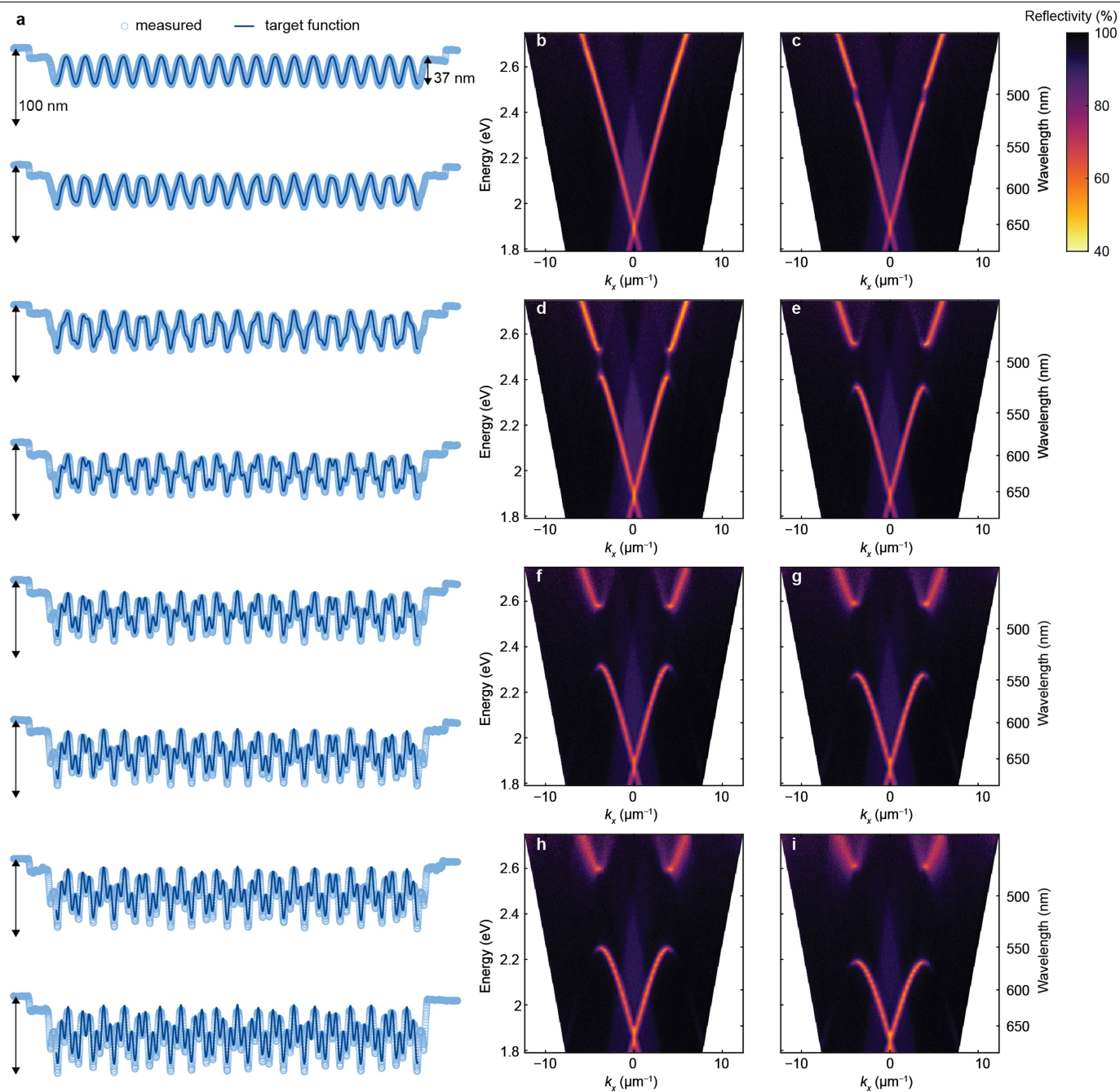
Extended Data Fig. 4 | Further analysis of the Ag Fourier surfaces in Fig. 1. **a, c, e,** Measured (AFM) and targeted surface topographies for the same sinusoidal structures as in Fig. 1a, d and g (blue) and their ‘binarized’ versions (red). The data for the Fourier surfaces represent half of the scans shown in Fig. 1b, e, h. The scan lengths for the binarized versions are 5.9 μm , 6.0 μm and 5.5 μm , respectively. For each Fourier surface, a binarized profile was obtained using a published thresholding procedure (see Methods). These binarized structures were then fabricated in a Si substrate using electron-beam lithography and etching. Ag replicas were obtained by templating (see Methods). The depth scale bars are 50 nm, 65 nm and 60 nm for both structures in **a, c** and **e**, respectively. **b, d, f,** Comparison of experimental

angle-resolved reflectivity spectra measured for the sinusoidal surfaces shown in **a, c** and **e** (left) and their binarized versions (right). The data for the sinusoids are the same as the left sides of Fig. 1c, f, i. The optical responses of the binarized gratings are clearly corrupted by the unwanted spatial frequencies in the structure. **g–i,** Normalized line cuts (orange curves) through the reflectivity data shown in the left panels in **b, d** and **f** at 500 nm, 600 nm and 600 nm, respectively. The black curves show the predicted reflectivity versus the absolute value of the in-plane wavevector, $|k_x|$ from our model (see Methods). The comparison reveals good agreement between the model and the data without any adjustable parameters (other than the normalization). For all structural design parameters, see Extended Data Table 1.



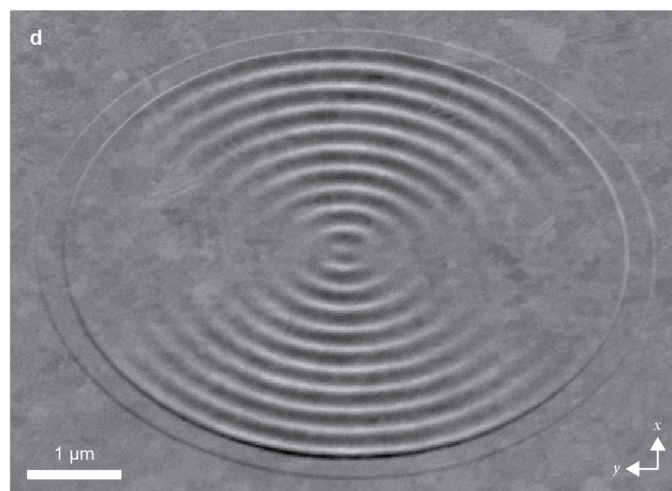
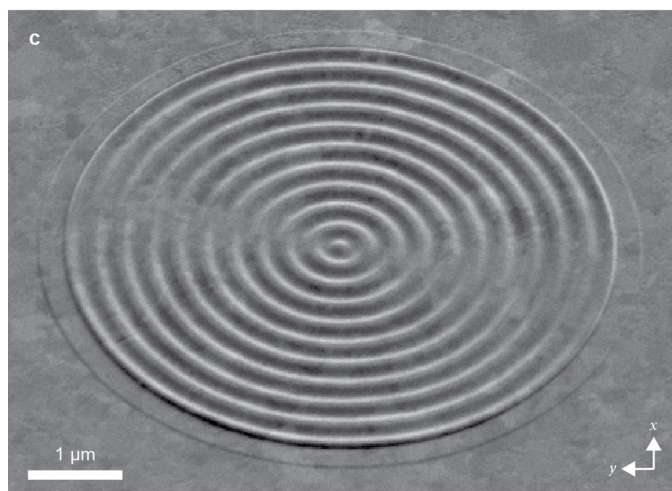
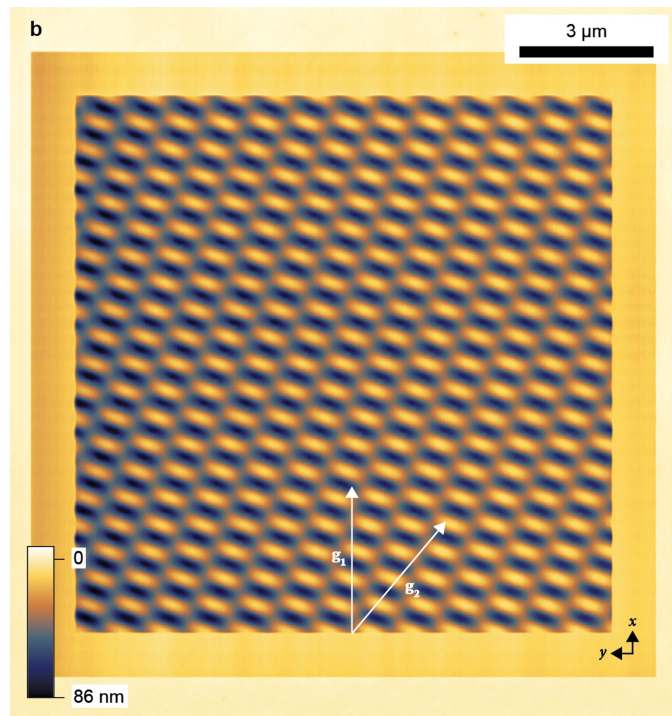
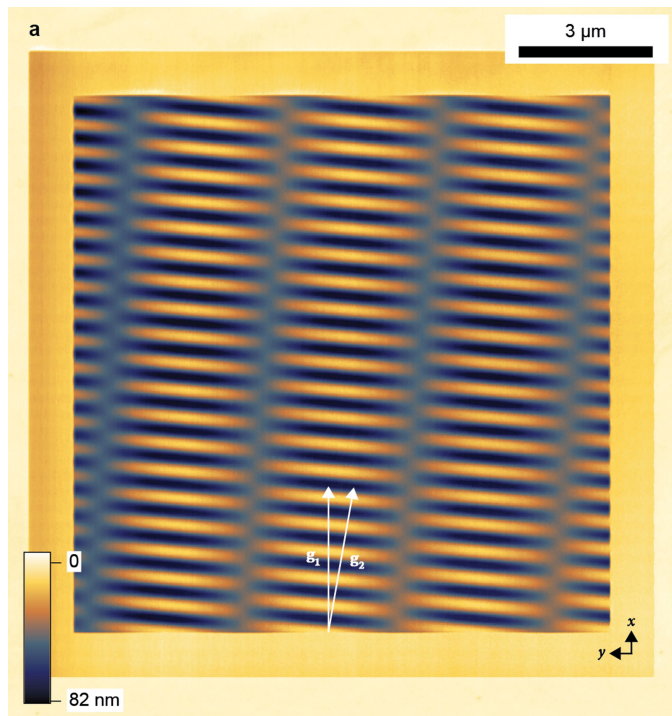
Extended Data Fig. 5 | Control of 'dark' band edges in two-component sinusoidal gratings. **a**, Comparisons of the measured (light blue points) and targeted surface topographies (dark blue lines) in the polymer surface, measured during patterning. Scan lengths are $11.5 \mu\text{m}$. The left grating has the height profile $f(x) = A_1 \cos(gx + \pi) + (A_1/2) \cos(2gx + \varphi_2) - \Delta$ with $\varphi_2 = \pi$. The grating on the right has the same $f(x)$ except $\varphi_2 = 0$. **b**, The measured reflectivity

in k -space (as in Fig. 1) for Ag gratings templated from the structures in **a**. In both the left and right gratings, a stopband opens near 1.9 eV, but the choice of phase can control whether an optically dark state exists at the lower (left) or upper (right) band edge. The band edge with the optically dark state is marked with white arrows. For all structural design parameters, see Extended Data Table 1.



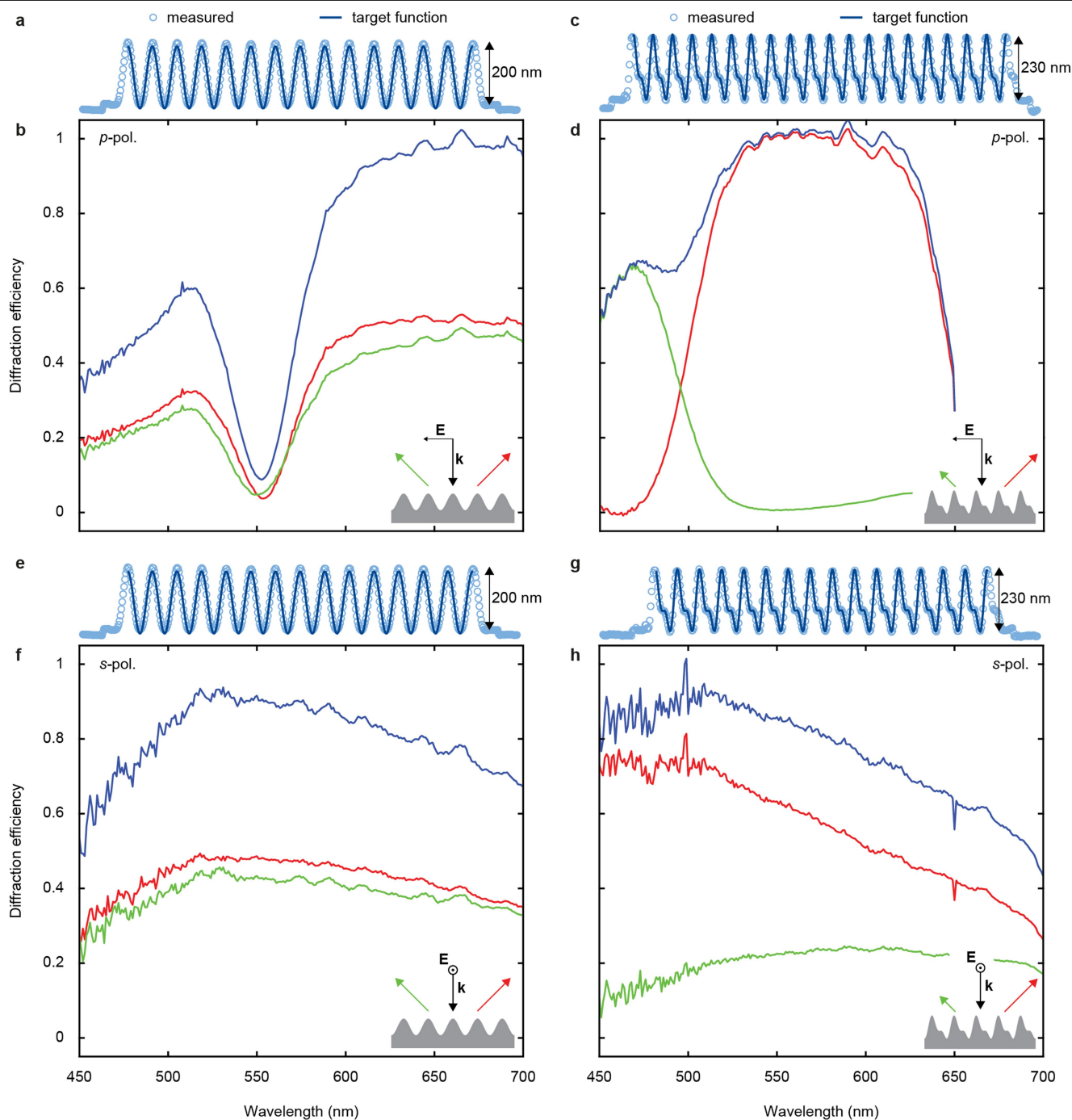
Extended Data Fig. 6 | Control of stopband width in two-component sinusoidal gratings. **a**, Comparisons of the measured (light blue points) and targeted surface topographies (dark blue lines) in the polymer surfaces, measured during patterning, for structures exhibiting a single stopband. Scan lengths are $14.5\ \mu\text{m}$ and the left vertical scale bar is $100\ \text{nm}$ for all scans. From top to bottom: a series of two-component sinusoidal gratings, where

$A_1 = 18.5\ \text{nm}$, $A_1 = 620\ \text{nm}$, A_2 is varied and $A_2 = 230\ \text{nm}$. A_2 has values of $0\ \text{nm}$, $2.5\ \text{nm}$, $5\ \text{nm}$, $10\ \text{nm}$, $15\ \text{nm}$, $18\ \text{nm}$, $20\ \text{nm}$ and $25.1\ \text{nm}$. **b–i**, Measured plasmonic dispersion diagrams for Ag gratings templated from the profiles in **a**, from top to bottom, respectively. The width of the stopband increases because A_2 is the amplitude of the Fourier component responsible for creating the plasmonic stopband. For all structural design parameters, see Extended Data Table 1.



Extended Data Fig. 7 | Fourier surface patterns. **a.** Measured topography (obtained during patterning) of the polymer film (PMMA/MA; see Methods) used to template the structure in Fig. 2a. The two spatial-frequency vectors \mathbf{g}_1 and \mathbf{g}_2 that define the surface profile are overlaid on the pattern. Here, \mathbf{g}_1 and \mathbf{g}_2 have the same magnitude $g_1 = g_2 = 2\pi/600$ nm, and \mathbf{g}_2 is rotated -10° from \mathbf{g}_1 , where \mathbf{g}_1 lies along \hat{x} . **b.** As in **a**, but the template corresponding to the structure in Fig. 2b. Again, \mathbf{g}_1 and \mathbf{g}_2 have the same magnitude $g_1 = g_2 = 2\pi/600$ nm, but \mathbf{g}_2 is

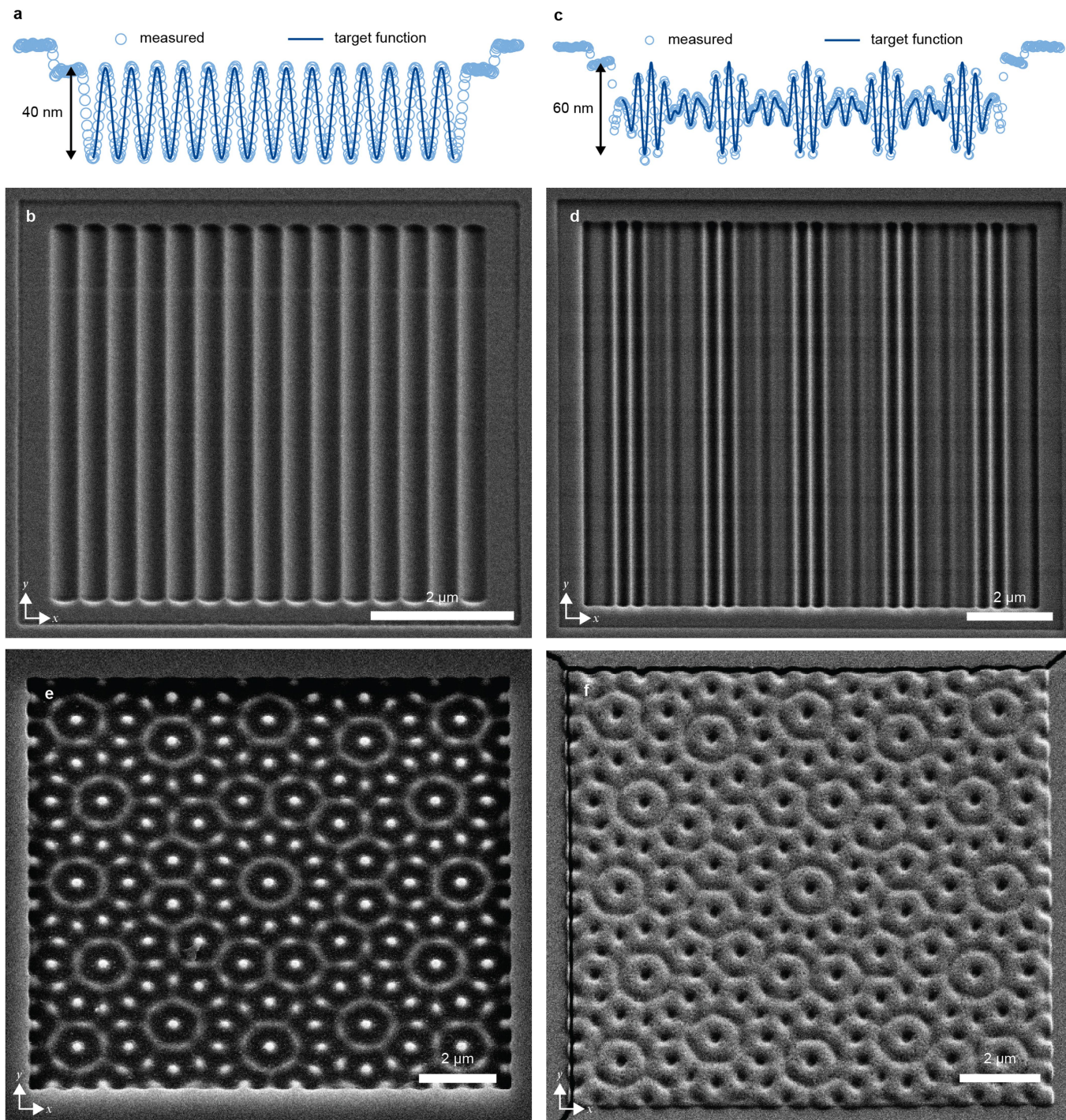
rotated -40° from \mathbf{g}_1 , where \mathbf{g}_1 lies along \hat{x} . **c.** SEM (45° tilt) of a circular sinusoidal Ag grating with $\lambda = 600$ nm. **d.** SEM (45° tilt) of two superimposed circular sinusoidal gratings, as in **c**, each with $\lambda = 600$ nm. The centre of one grating is translated $+150$ nm and the other -150 nm in \hat{y} from the origin in the middle of the pattern. The spatial interference results in a moiré pattern with broken circular symmetry. For all structural design parameters, see Extended Data Table 1.



Extended Data Fig. 8 | Efficient diffraction from photonic Fourier surfaces.

a, Comparison of the measured (AFM) and targeted surface topography (accounting for a slight distance miscalibration and depth nonlinearity in the thermal scanning probe) for a deeper sinusoidal Ag grating designed for efficient optical diffraction. The scan length is $18.5 \mu\text{m}$. **b**, Measured diffraction efficiency as a function of photon wavelength for the grating profile shown in **a**, for p-polarized illumination at normal incidence. The inset illustrates how incident photons (black arrow with wavevector \mathbf{k} and electric field \mathbf{E} indicated) diffract symmetrically into the +1 (red arrow) and -1 (green arrow) diffraction orders. The red and green curves correspond to the +1 and -1 diffracted intensities, respectively, normalized to the intensity reflected from

an unpatterned flat reference spot on the same Ag sample. The sum of the red and green curves (blue line) peaks at about 97%. Owing to fluctuations in the collected diffraction intensity, the measured efficiencies have an estimated error of $\pm 5\%$. We also note that our measurement does not account for reflection losses in the Ag (a few per cent). **c**, As in **a**, but for a two-component sinusoidal Ag grating where the relative phase between the two components is chosen to break the mirror symmetry of the structure about the y - z plane. **d**, As in **b**, but now the broken symmetry causes nearly all of the incident light to be diffracted into the +1 diffraction order (red curve) for a given wavelength range. **e-h**, As in **a-d**, but for s-polarized illumination at normal incidence. For all structural design parameters, see Extended Data Table 1.



Extended Data Fig. 9 | SiN_x and TiO_2 Fourier surfaces. **a**, Comparison of the measured (AFM) and targeted surface topography (accounting for a slight distance miscalibration in the thermal scanning probe) for a single sinusoid in SiN_x , transferred via reactive-ion etching (see Methods). Scan length is $11.3 \mu\text{m}$. **b**, SEM (30° tilt) of the same structure in **a**. The final profile in SiN_x has a measured RMS error of 2.5 nm using the same methodology as in Extended Data Fig. 2. **c**, As in **a**, but for a three-component SiN_x grating. Scan length

is $14.8 \mu\text{m}$. **d**, As in **b**, but for the structure in **c**. The final profile in SiN_x has a measured RMS error of 3.9 nm using the same methodology as in Extended Data Fig. 2. **e**, SEM (30° tilt) of a 12-fold rotationally symmetric quasicrystal, as in Fig. 3d, transferred from the patterned polymer into Si via inductively coupled plasma etching (see Methods). **f**, SEM (30° tilt) of the pattern in **e** transferred into a TiO_2 thin film via template stripping (see Methods). For all structural design parameters, see Extended Data Table 1.

Article

Extended Data Table 1 | Design parameters for Fourier surfaces

Parameters											Height profile	
Figure	A_1 (nm)	A_2 (nm)	A_3 (nm)	Λ_1 (nm)	Λ_2 (nm)	Λ_3 (nm)	φ_1 (deg)	φ_2 (deg)	φ_3 (deg)	Δ (nm)	$f(x)$	
Fig. 1a	25.0	–	–	600	–	–	180	–	–	35.0	$\sum_i A_i \cos(g_i x + \varphi_i) - \Delta$	
Fig. 1d	18.1	14.3	–	600	475	–	0	0	–	42.3		
Fig. 1g	18.4	7.0	6.4	600	230	210	0	0	0	41.8		
ED Fig. 5	19.3	9.6	–	620	310	–	180	180	–	24.4		
								0		38.9		
ED Fig. 6	18.5	0 to 25.1	–	620	230	–	0	0	–	28.0 to 53.1		
Fig. 4b	12.0	12.0	12.0	620	520	445	0	0	0	45.9		
ED Fig. 8a,e	100	–	–	1000	–	–	180	–	–	110		
ED Fig. 8c	88.6	44.3	–	800	400	–	90	90	–	125		
ED Fig. 8g	88.6	44.3	–	900	450	–	90	90	–	125		
ED Fig. 9b	25.0	–	–	400	–	–	180	–	–	35.0		
ED Fig. 9d	14.1	11.8	10.1	414	347	297	0	0	0	45.8		
Figure	i	A_i (nm)	Λ_i (nm)	φ_i (deg)	$\theta_{1,7}$ (deg)	$\theta_{2,8}$ (deg)	$\theta_{3,9}$ (deg)	$\theta_{4,10}$ (deg)	$\theta_{5,11}$ (deg)	$\theta_{6,12}$ (deg)	Δ (nm)	$f(x, y)$
Fig. 2a	1,2	17.5	600	0	0	-10	–	–	–	–	45.0	$\sum_i A_i \cos[g_i(x \cos \theta_i + y \sin \theta_i) + \varphi_i] - \Delta$
Fig. 2b	1,2	17.5	600	0	0	-40	–	–	–	–	45.0	
Fig. 3a	1,2,3	15.6	600	0	0	60	120	–	–	–	56.7	
Fig. 3d	1–6	10.0	600	0	0	30	60	90	120	150	70.0	
Fig. 4e	1–6	5.6	700	0	0	30	60	90	120	150	77.3	
	7–12	5.6	308	0	0	30	60	90	120	150	77.3	
ED Fig. 9e,f	1–6	11.1	615	0	0	30	60	90	120	150	76.7	
Figure	i	A_1 (nm)	A_2 (nm)	Λ_1 (nm)	Λ_2 (nm)	φ_1 (deg)	φ_2 (deg)	Δ (nm)	r_1 (nm)	r_2 (nm)	$f(r, \theta)$	
ED Fig. 7c	1	35.0	–	600	–	180	–	45	0	–	$\sum_i A_i \cos(g_i r - r_i + \varphi_i) - \Delta$	
ED Fig. 7d	1,2	17.5	17.5	600	600	180	0	45	-150 \hat{y}	150 \hat{y}		
Figure	A (nm)	L (nm)	Δ (nm)	$f(r)$								
Fig. 2e	35.0	1581	45.0	$A \sin \left[\pi \left(\frac{r}{L} \right)^2 \right] - \Delta$								

Design parameters for all Fourier surfaces demonstrated in this work. The functions are defined for the design to be patterned in the polymer surface, where x and y lie in-plane and z is perpendicular (pointing away from the substrate). A right-handed coordinate system is used with the origin placed in the middle of the pattern in both the x and y directions. In these formulas, the height of the surface is defined relative to the unpatterned flat surface where $z = 0$. All A_i and Δ_i (Λ_i) have been rounded to the nearest 0.1 nm (1.0 nm). Analysis of the measured topographies for templated Ag gratings shows that the Λ_i values are consistently about 2% larger than the design value (Extended Data Fig. 2), attributed to a distance miscalibration in the thermal scanning probe. See Methods.